Mathematics

AIMS Mathematics, 10(3): 5830−5858.
DOI: 10.3934/math.2025268
Received: 07 December 2024
Revised: 10 January 2025
Accepted: 18 February 2025
Published: 17 March 2025

https://www.aimspress.com/journal/Math

Research article

Exothermic thermosolutal convection in a nanofluid-filled square cavity with a rotating Z-Fin: ISPH and AI integration

Kuiyu Cheng[1], Abdelraheem M. Aly[2,*], Nghia Nguyen Ho[1], Sang-Wook Lee[1], Andaç Batur Çolak[3] and Weaam Alhejaili[4]

[1] School of Mechanical Engineering, University of Ulsan, Ulsan, South Korea
[2] Department of Mathematics, College of Science, King Khalid University, Abha, Saudi Arabia
[3] Department of Information Systems and Technologies, Niğde Ömer Halisdemir University, 51240 Niğde, Türkiye
[4] Department of Mathematical Sciences, College of Science, Princess Nourah bint Abdulrahman University, P.O. Box 84428, Riyadh 11671, Saudi Arabia

* **Correspondence:** Email: ababdallah@kku.edu.sa, Tel: +966-551323276.

Abstract: This study explores the combined effects of exothermic chemical reactions and Cattaneo–Christov heat flux on thermosolutal convection within a nanofluid-filled square cavity containing a rotating Z-shaped fin. The incompressible smoothed particle hydrodynamics (ISPH) approach was employed, utilizing boundary particle renormalization to accurately model boundary conditions. An artificial neural network (ANN) model, trained on ISPH simulation data, predicted the average Nusselt number (Nu_{avg}) and average Sherwood number (Sh_{avg}) with high accuracy. A dataset comprising 56 data points was used, from which 40 data points were used for training, 8 for validation, and 8 for testing. The Z-shaped fin, centrally positioned, rotates at a fixed angular velocity, maintaining lower temperature and concentration levels, while the cavity's vertical walls exhibit elevated thermal and solutal conditions. Results indicate that the Z-shaped fin's geometry, exothermic reaction rates, and magnetic field strength significantly influence heat and mass transfer and fluid dynamics. For instance, increasing the Hartmann number (Ha) from 0 to 50 decreased nanofluid velocity by 61.99%, while Nu_{avg} and Sh_{avg} were reduced by 16.87% and 11.81%, respectively. Additionally, increasing the nanoparticle volume fraction from 0 to 0.15 enhanced Nu_{avg} by 22.43% and Sh_{avg} by 116.3%. The ANN model, employing the Levenberg–Marquardt algorithm, achieved a coefficient of determination $R = 0.99994$ and a mean squared error $\text{MSE} = 4.21 \times 10^{-6}$, demonstrating its reliability in predicting thermal performance. These findings underscore the study's relevance to applications such as energy systems, refrigeration, and heat exchangers.

Keywords: Cattaneo–Christov heat flux; exothermic chemical reaction; ISPH method; magnetic field; rotating Z-shaped fin
Mathematics Subject Classification: 76D05, 76W05, 80A20, 35Q79, 68T07

1. Introduction

Convection heat transfer in ventilated cavities has numerous applications in industrial systems for building ventilation, thermal control of electronic devices, and removal of contaminated particles [1,2]. In addition, exothermic chemical reactions play an important role in chemical fractionation, combustion, explosions, oil recovery, and moisture transfer in grain storage. Nanofluids are a combination of a host fluid and nano-sized metal particles [3]. Nanofluids are widely used in the cooling process of heat exchangers and electronic devices [4]. In particular, the analysis of heat transfer and chemical reactions of nanofluids is expected to receive more attention in the near future because of its practical applications in petroleum extraction, nuclear reactors, evaporation, chemistry, and refrigeration industries [5−15]. Nanofluids—suspensions of nano-sized particles in base fluids—are drawing wide interest for their superior heat transfer capabilities. Early experiments revealed discrepancies between predicted and measured heat transfer coefficients (Yang et al. [5]). Nonetheless, subsequent findings underscore their broad potential. Putra et al. [6] show that adding nanofluids and thermoelectric cooling "significantly enhances heat removal". Mahian et al. [7] report that nanofluids "boost solar collector efficiency", while Rashidi et al. [8] highlight their impact on condensation and evaporation processes. In porous media, Khanafer and Vafai [9] call nanofluids "an effective means" to enhance convective heat transfer. Alhuyi Nazari et al. [10] confirm their ability to lower thermal resistance in heat pipes. Sajid and Ali [11], however, emphasize "key challenges", including high pumping power. Wahab et al. [12] demonstrate "notable performance gains" in solar energy systems, given proper stability management. Saidina et al. [13] confirm strong cooling effects for electronics, stressing the need for property optimization. Li et al. [14] propose neural networks for "accurate modeling" of nanofluid thermal behavior. Finally, Sheremet et al. [15] observes "substantial progress", while urging further research on stability and standardization. Mathematically, the chemical reaction is characterized by Arrhenius kinetics [16,17]. Rahman et al. [18] explored how exothermic reactions, modeled by Arrhenius kinetics, influence natural convection in a porous square cavity with nanofluids, utilizing the Galerkin finite element method (GFEM). Raees-ul-Haq [19] simulated the effects of exothermic reactions on free convection within a magnetized nanofluid-filled triangular porous cavity. Similarly, Hasan et al. [20] applied GFEM to examine magnetohydrodynamics (MHD) driven convective flows in a cavity influenced by such chemical reactions. Magnetic field and nanofluid flow interactions within cavities are valuable in engineering applications, such as refrigeration and cooling systems [21−23]. Aly et al. [24] used the incompressible smoothed particle hydrodynamics (ISPH) approach to examine how varying magnetic fields and helical structures affect convection within a ferrofluid cavity. Aly [25] also leveraged ISPH to simulate the thermosolutal convection in a nanofluid cavity, highlighting magnetic and thermal diffusion effects. Introduced by Gingold and Monaghan [26] and Lucy [27], the meshless Lagrangian nature of the SPH method has led to its widespread use in handling complex fluid dynamics scenarios, such as multi-phase flows, free surfaces, strong nonlinearities, and turbulent behaviors like jet impingement and nozzles [28−32]. Violeau and Issa [28] provided an extensive overview of the SPH method's capabilities in modeling turbulent, complex free-surface flows, highlighting its potential for simulating challenging fluid dynamics scenarios. Qiang et

al. [29] utilized the SPH approach to study two-dimensional droplet collisions, effectively addressing the complexities of multi-phase flows with large density variations. Aly et al. [30] applied the ISPH method to investigate mixed convection in an inclined cavity with sinusoidal heated walls, advancing the understanding of convective flows in confined spaces. Garoosi and Shakibaeinia [31] proposed a refined high-order ISPH approach for simulating free-surface flows and heat transfer, enhancing accuracy in complex fluid–thermal interactions. More recently, Shimizu et al. [32] examined the applicability of a higher-order consistent ISPH method, assessing its performance in detailed simulations for ocean and polar engineering applications. To enhance heat and mass transfer in closed systems, heat exchangers and solar cells frequently utilize fins or textured surfaces. Saeid [33] investigated the influence of fin geometry on heating within a square cavity. Aly and El-Sapa [34] employed ISPH to analyze MHD thermosolutal convection in a nanofluid cavity featuring a rotating cylinder and a cross-shaped fin. Meanwhile, El Moutaouakil et al. [35] studied the impact of vertical fins on natural convection within cavities. Recent studies have explored the application of artificial neural networks (ANNs) to heat and mass transfer in cavities, demonstrating the potential of these models to accurately predict complex thermal and solutal behaviors under various boundaries and initial conditions. ANNs are a powerful computational tool in various fields due to their ability to represent complex nonlinear interactions and rapidly process large datasets. They are particularly useful for complex boundary conditions or multi-physics phenomena. ANNs can accurately forecast system behavior, improve performance, and provide real-time solutions. They have been used to predict thermal conductivity, examine fluid flow properties, and analyze convection in heat exchangers. Their generalization capability makes them an ideal complement to conventional numerical techniques like ISPH. This study shows that combining ANNs with ISPH improves accuracy and computing efficiency in addressing exothermic thermosolutal convection in a nanofluid-filled square cavity. ANN models have become instrumental in handling nonlinear interactions and diverse parameters like temperature, concentration, velocity, and Nusselt and Sherwood numbers ([36−38]). Lagaris et al. [39] utilized an ANN model to solve ordinary and partial differential equations, showing its effectiveness for complex equations. Díaz et al. [40] applied ANNs to simulate heat exchanger performance, improving predictive accuracy. Varol et al. [41] predicted natural convection flow and temperature in a triangular enclosure using ANN and ANFIS models. Motahar [42] used ANN to estimate non-Newtonian nanofluid behavior with phase change materials. Alhejaili et al. [43] combined ANN with ISPH to study heat and mass transfer in nano-encapsulated materials within complex cavities. Elshehabey et al. [44] integrated ANN and ISPH for modeling thermal radiation in porous, finned cavities. Lastly, Abdelsalam et al. [45] applied AI-powered ANN for bioconvection analysis involving nano-encapsulation and oxytactic microorganisms. This research explores the effects of exothermic reactions, magnetic fields, and Cattaneo–Christov heat flux on thermosolutal convection by applying the ISPH method within a nanofluid-filled cavity containing a rotating Z-shaped fin. The ANN model is also employed to precisely estimate average Nusselt and Sherwood numbers, providing deeper insights into the heat and mass transfer processes in this setup.

2. Mathematical analysis

2.1. Physical model and governing equations

The initial setup of the rotating Z-shaped fin for thermosolutal convection analysis is depicted in Figure 1. The fin rotates with a circular velocity, represented by $\mathbf{V} = \omega(\mathbf{r} - \mathbf{r}_0)$, and is maintained at a specified low temperature (T_c) and concentration (C_c). The cavity's vertical walls are maintained at

elevated temperature (T_h) and concentration (C_h), while the horizontal walls are adiabatic. The flow is modeled under the following assumptions:

- The flow is incompressible, laminar, and time dependent.
- The Boussinesq approximation is applied, accounting for buoyancy effects due to temperature and concentration variations.
- The fluid is Newtonian, and the nanofluid properties are assumed to be constant, except for density in the buoyancy term.
- Heat and mass transfer are driven by both thermal and solutal gradients.
- The governing equations are formulated in a Cartesian coordinate system (x, y) to represent the geometry of the square cavity.
- The rotating Z-shaped fin is modeled as a rigid body with no deformation.

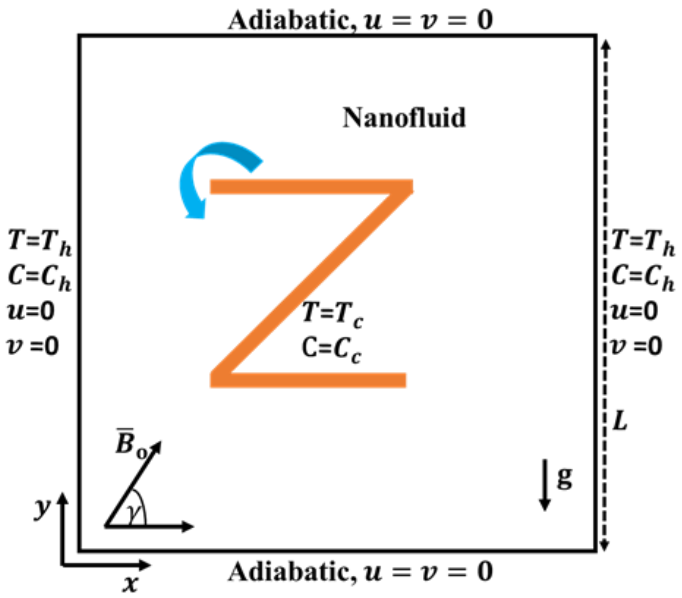

Figure 1. Diagram of a rotating Z-shaped fin, illustrating the rotational direction in thermosolutal convection studies.

The dimensional form of the governing equations, as outlined in references [46–48], is:

$$\frac{\partial u}{\partial x} + \frac{\partial v}{\partial y} = 0, \tag{1}$$

$$\frac{du}{dt} = -\frac{1}{\rho_{\mathrm{nf}}}\frac{\partial p}{\partial x} + \frac{\mu_{\mathrm{nf}}}{\rho_{\mathrm{nf}}}\left(\frac{\partial^2 u}{\partial x^2} + \frac{\partial^2 u}{\partial y^2}\right) - \frac{\sigma_{\mathrm{nf}} B_0^2}{\rho_{\mathrm{nf}}}(u \sin^2\gamma - v \sin\gamma \cos\gamma), \tag{2}$$

$$\frac{dv}{dt} = -\frac{1}{\rho_{\mathrm{nf}}}\frac{\partial p}{\partial y} + \frac{\mu_{\mathrm{nf}}}{\rho_{\mathrm{nf}}}\left(\frac{\partial^2 v}{\partial x^2} + \frac{\partial^2 v}{\partial y^2}\right) + \frac{(\rho\beta_T)_{\mathrm{nf}}}{\rho_{\mathrm{nf}}}\,\mathrm{g}(T - T_c) + \frac{(\rho\beta_C)_{\mathrm{nf}}}{\rho_{\mathrm{nf}}}\,\mathrm{g}(C - C_c)$$
$$-\frac{\sigma_{\mathrm{nf}} B_0^2}{\rho_{\mathrm{nf}}}(v \cos^2\gamma - u \sin\gamma \cos\gamma), \tag{3}$$

$$\frac{dT}{dt} = \nabla \cdot (\alpha_{\mathrm{nf}} \nabla T) + \frac{1}{(\rho C_P)_{\mathrm{nf}}} \nabla \cdot (D_1 \nabla C) + \frac{1}{(\rho C_P)_{\mathrm{nf}}} \frac{Q k_o a}{e^{\frac{E}{RT}}}$$

$$-\delta_1\left(u\frac{\partial T}{\partial x}\frac{\partial u}{\partial x}+v\frac{\partial T}{\partial y}\frac{\partial v}{\partial y}+u^2\frac{\partial^2 T}{\partial x^2}+v^2\frac{\partial^2 T}{\partial y^2}+2uv\frac{\partial^2 T}{\partial x\partial y}+u\frac{\partial T}{\partial y}\frac{\partial v}{\partial x}+v\frac{\partial T}{\partial x}\frac{\partial u}{\partial y}\right), \tag{4}$$

$$\frac{dC}{dt}=\nabla\cdot(D_2\,\nabla T)+\nabla\cdot(D_m\,\nabla C). \tag{5}$$

The subsequent dimensionless variables [46–48] are substituted into Eqs (1)–(5) as:

$$X=\frac{x}{L},\qquad Y=\frac{y}{L},\qquad \tau=\frac{t\alpha_{\mathrm{f}}}{L^2},\qquad U=\frac{uL}{\alpha_{\mathrm{f}}},\qquad V=\frac{vL}{\alpha_{\mathrm{f}}},\quad \alpha_f=\frac{k_{\mathrm{f}}}{(\rho C_P)_{\mathrm{f}}}$$

$$P=\frac{pL^2}{\rho_{\mathrm{nf}}\,\alpha_{\mathrm{f}}^2},\theta=\frac{T-T_c}{T_h-T_c},\Phi=\frac{C-C_c}{C_h-C_c}. \tag{6}$$

The dimensionless equations [46–48] are obtained as:

$$\frac{\partial U}{\partial X}+\frac{\partial V}{\partial Y}=0, \tag{7}$$

$$\frac{dU}{d\tau}=-\frac{\partial P}{\partial X}+\frac{\mu_{\mathrm{nf}}}{\rho_{\mathrm{nf}}\alpha_{\mathrm{f}}}\left(\frac{\partial^2 U}{\partial X^2}+\frac{\partial^2 U}{\partial Y^2}\right)-\frac{\sigma_{\mathrm{nf}}\,\rho_f}{\sigma_{\mathrm{f}}\,\rho_{nf}}\,\mathrm{Ha}^2\,\mathrm{Pr}(\mathrm{U}\sin^2\gamma\;-\mathrm{V}\sin\gamma\cos\gamma), \tag{8}$$

$$\frac{dV}{d\tau}=-\frac{\partial P}{\partial Y}+\frac{\mu_{\mathrm{nf}}}{\rho_{\mathrm{nf}}\alpha_{\mathrm{f}}}\left(\frac{\partial^2 V}{\partial X^2}+\frac{\partial^2 V}{\partial Y^2}\right)+\frac{(\rho\beta)_{\mathrm{nf}}}{\rho_{\mathrm{nf}}\,\beta_{\mathrm{f}}}Ra\,\mathrm{Pr}(\theta+N\Phi)$$

$$-\frac{\sigma_{\mathrm{nf}}\,\rho_f}{\sigma_{\mathrm{f}}\,\rho_{nf}}\,\mathrm{Ha}^2\,\mathrm{Pr}(\mathrm{V}\cos^2\gamma\;-\mathrm{U}\sin\gamma\cos\gamma), \tag{9}$$

$$\frac{d\theta}{d\tau}=\frac{1}{(\rho C_P)_{\mathrm{nf}}}\,Du\left(\frac{\partial^2\Phi}{\partial X^2}+\frac{\partial^2\Phi}{\partial Y^2}\right)+\frac{\alpha_{nf}}{\alpha_f}\left(\frac{\partial^2\theta}{\partial X^2}+\frac{\partial^2\theta}{\partial Y^2}\right)+\frac{1}{(\rho C_P)_{\mathrm{nf}}}F_k e^{\theta}$$

$$-\delta_C\left(U\frac{\partial\theta}{\partial X}\frac{\partial U}{\partial X}+V\frac{\partial\theta}{\partial Y}\frac{\partial V}{\partial Y}+U^2\frac{\partial^2\theta}{\partial X^2}+V^2\frac{\partial^2\theta}{\partial Y^2}+2UV\frac{\partial^2\theta}{\partial X\partial Y}+U\frac{\partial\theta}{\partial Y}\frac{\partial V}{\partial X}+V\frac{\partial\theta}{\partial X}\frac{\partial U}{\partial Y}\right), \tag{10}$$

$$\frac{d\Phi}{d\tau}=Sr\left(\frac{\partial^2\theta}{\partial X^2}+\frac{\partial^2\theta}{\partial Y^2}\right)+\frac{1}{Le}\left(\frac{\partial^2\Phi}{\partial X^2}+\frac{\partial^2\Phi}{\partial Y^2}\right), \tag{11}$$

where $Sr=\frac{D_2}{\alpha_f}\left(\frac{(T_h-T_c)}{(C_h-C_c)}\right)$ is the Soret number, $Du=\frac{D_1}{\alpha_f}\left(\frac{(C_h-C_c)}{(T_h-T_c)}\right)$ is the Dufour number, $\delta_C=\frac{\nu_f\delta_1}{L^2}$ is a parameter of Cattaneo–Christov heat flux, $Ha=\sqrt{\frac{\sigma_{\mathrm{f}}}{\mu_{\mathrm{f}}}}\,B_0L$ is the Hartmann number, $Ra=\frac{\mathrm{g}\beta_T(T_h-T_c)L^3}{\nu_f\alpha_{\mathrm{f}}}$ is Rayleigh's number, $Pr=\frac{\nu_f}{\alpha_f}$ is the Prandtl number, $Le=\frac{\alpha_f}{D_m}$ is the Lewis number, and $N=\frac{\beta_C(C_h-C_c)}{\beta_T(T_h-T_c)}$ is a buoyancy ratio.

2.2. Dimensionless boundary conditions

The boundary conditions for the model are defined as follows:

Vertical walls: Temperature (θ) and concentration (Φ) are set to 1, with no-slip velocity conditions ($U=0,\ V=0$).

Horizontal walls: Adiabatic and impermeable conditions are applied, ensuring no heat or mass flux ($\frac{\partial\theta}{\partial Y}=0,\ \frac{\partial\Phi}{\partial Y}=0$) and no-slip velocity ($U=0,\ V=0$). (12)

Inner Z-shaped fin: The fin rotates, imposing velocity conditions ($U=U_{\mathrm{rot}},\ V=V_{\mathrm{rot}}$) and maintaining lower temperature and concentration levels ($\theta=0,\ \Phi=0$).

The mean values for Nusselt and Sherwood numbers are:

$$\overline{Nu} = -\int_0^1 \frac{k_{\mathrm{nf}}}{k_{\mathrm{f}}}\left(\frac{\partial\theta}{\partial X}\right)dY, \tag{13}$$

$$\overline{Sh} = -\int_0^1 \left(\frac{\partial\Phi}{\partial X}\right)dY. \tag{14}$$

2.3. Nanofluid properties

The nanofluid properties are determined using the following equations [49–51]:

$$\rho_{\mathrm{nf}} = \rho_{\mathrm{f}} + \phi\left(\rho_{\mathrm{np}} - \rho_{\mathrm{f}}\right) \tag{15}$$

$$\left(\rho C_p\right)_{\mathrm{nf}} = \left(\rho C_p\right)_{\mathrm{f}} + \phi\left(\left(\rho C_p\right)_{\mathrm{np}} - \left(\rho C_p\right)_{\mathrm{f}}\right) \tag{16}$$

$$(\rho\beta)_{\mathrm{nf}} = (\rho\beta)_{\mathrm{f}} + \phi\left((\rho\beta)_{\mathrm{np}} - (\rho\beta)_{\mathrm{f}}\right) \tag{17}$$

$$\sigma_{\mathrm{nf}} = \left(\frac{3\phi(\sigma_{\mathrm{np}}/\sigma_{\mathrm{f}}-1)}{(\sigma_{\mathrm{np}}/\sigma_{\mathrm{f}}+2)-(\sigma_{\mathrm{np}}/\sigma_{\mathrm{f}}-1)\phi} + 1\right)\sigma_{\mathrm{f}} \tag{18}$$

$$\alpha_{\mathrm{nf}} = \frac{k_{\mathrm{nf}}}{\left(\rho C_p\right)_{\mathrm{nf}}} \tag{19}$$

$$k_{\mathrm{nf}} = \left(k_{\mathrm{np}} + 2k_{\mathrm{f}}\right) + \phi\frac{\left((k_{\mathrm{np}}+2k_{\mathrm{f}})k_{\mathrm{f}}-2\phi(k_{\mathrm{f}}-k_{\mathrm{np}})k_{\mathrm{f}}\right)}{(k_{\mathrm{f}}-k_{\mathrm{np}})} \tag{20}$$

$$\mu_{\mathrm{nf}} = \frac{\mu_{\mathrm{f}}}{(1-\phi)^{2.5}}. \tag{21}$$

3. The SPH formulation

The core concept of the SPH approximation is:

$$\langle f(\boldsymbol{r}_i)\rangle = \frac{1}{\xi_i}\sum_j \frac{m_j}{\rho_j} f(\boldsymbol{r}_j) W(\boldsymbol{r}_{ij}, h). \tag{22}$$

Here, W is a quintic smoothing function:

$$W(q,h) = \kappa\begin{cases}(2-q)^5 - 16(1-q)^5 & 0 \le q \le 1\\ (2-q)^5 & 1 < q \le 2,\\ 0 & q > 2\end{cases} \tag{23}$$

where $\kappa = \frac{3}{16\,\pi\,h^2}$, and $q = \boldsymbol{r}_{ij}/h$ with h as a smoothing length.
The renormalization factor ξ_i is defined as [47,52]:

$$\xi_i = \int_{\Omega_i} W(|\boldsymbol{r}_{ab}|)d\Omega(\boldsymbol{r}_j). \tag{24}$$

The first derivative is:

$$\nabla\xi_{ie} = -\int_{e_1}^{e_2} \boldsymbol{n}(\boldsymbol{r}_j)\, W(\boldsymbol{r}_{ij})d\Gamma(\boldsymbol{r}_j). \tag{25}$$

Figure 2 shows the initial schematic description of the SPH discretization of a target geometry and kernel (smoothing) function. The initial geometry is discretized into uniform nodes (particles). Any hydrodynamic function is calculated according to the SPH approximation.

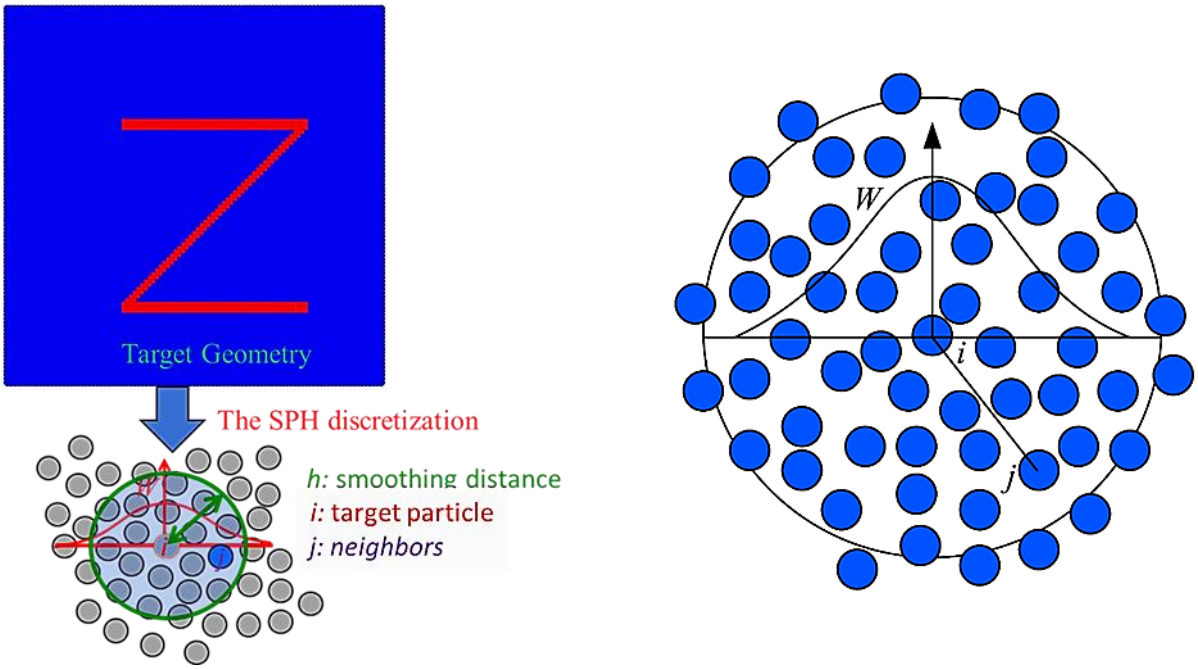

(a) (b)

Figure 2. Initial schematic description of (a) the SPH discretization of a target geometry and (b) the kernel (smoothing) function.

4. The ISPH method

The ISPH algorithm [46,47,53,54] is summarized in the following steps:
Step 1: Predict velocities.

$$U^* = U^n + \frac{\mu_{\rm nf}\,\Delta\tau}{\rho_{\rm nf}\alpha_{\rm f}}\left(\frac{\partial^2 U}{\partial X^2}+\frac{\partial^2 U}{\partial Y^2}\right)^n - \frac{\Delta\tau\sigma_{\rm nf}\,\rho_f}{\sigma_{\rm f}\,\rho_{nf}}\,{\rm Ha}^2\,{\rm Pr}(U^n\sin^2\gamma - V^n\sin\gamma\cos\gamma), \tag{26}$$

$$V^* = V^n + \frac{\mu_{\rm nf}\,\Delta\tau}{\rho_{\rm nf}\alpha_{\rm f}}\left(\frac{\partial^2 V}{\partial X^2}+\frac{\partial^2 V}{\partial Y^2}\right)^n + \frac{\Delta\tau\,(\rho\beta)_{\rm nf}}{\rho_{\rm nf}\,\beta_{\rm f}}Ra\,{\rm Pr}\,(\theta^n + N\Phi^n)$$

$$-\frac{\Delta\tau\sigma_{\rm nf}\,\rho_f}{\sigma_{\rm f}\,\rho_{nf}}\,{\rm Ha}^2\,{\rm Pr}(V^n\cos^2\gamma - U^n\sin\gamma\cos\gamma). \tag{27}$$

Step 2: Solve the pressure Poisson equation.

$$\nabla^2 P^{n+1} = \frac{1}{\Delta\tau}\left(\frac{\partial U^*}{\partial X}+\frac{\partial V^*}{\partial Y}\right). \tag{28}$$

Step 3: Correct velocities.

$$U^{n+1} = U^* - \Delta\tau\left(\frac{\partial P}{\partial X}\right)^{n+1}, \tag{29}$$

$$V^{n+1} = V^* - \Delta\tau\left(\frac{\partial P}{\partial Y}\right)^{n+1}. \tag{30}$$

Step 4: Update thermal and solutal equations.

$$\theta^{n+1} = \theta^n + \frac{\alpha_{nf}\,\Delta\tau}{\alpha_f}\left(\frac{\partial^2\theta}{\partial X^2} + \frac{\partial^2\theta}{\partial Y^2}\right)^n + \frac{\Delta\tau}{(\rho C_P)_{\mathrm{nf}}}\,Du\left(\frac{\partial^2\Phi}{\partial X^2} + \frac{\partial^2\Phi}{\partial Y^2}\right)^n$$

$$-\Delta\tau\,\delta_C\left(U\frac{\partial\theta}{\partial X}\frac{\partial U}{\partial X} + V\frac{\partial\theta}{\partial Y}\frac{\partial V}{\partial Y} + U^2\frac{\partial^2\theta}{\partial X^2} + V^2\frac{\partial^2\theta}{\partial Y^2} + 2UV\frac{\partial^2\theta}{\partial X\partial Y} + U\frac{\partial\theta}{\partial Y}\frac{\partial V}{\partial X} + V\frac{\partial\theta}{\partial X}\frac{\partial U}{\partial Y}\right)^n$$

$$+\frac{\Delta\tau}{(\rho C_P)_{\mathrm{nf}}}F_k e^{\theta^n}, \tag{31}$$

$$\Phi^{n+1} = \Phi^n + \Delta\tau\,Sr\left(\frac{\partial^2\theta}{\partial X^2} + \frac{\partial^2\theta}{\partial Y^2}\right)^n + \frac{\Delta\tau}{Le}\left(\frac{\partial^2\Phi}{\partial X^2} + \frac{\partial^2\Phi}{\partial Y^2}\right)^n. \tag{32}$$

Step 5: Update the position of particles.

$$\boldsymbol{r}^{n+1} = \Delta\tau\,\mathbf{U}^{n+1} + \boldsymbol{r}^n. \tag{33}$$

The shifting technique [55,56] is as follows:

$$\varphi_{i'} = \varphi_i + (\boldsymbol{\nabla}\varphi)_i \cdot (-\mathcal{D}\,\boldsymbol{\nabla}C) + \mathcal{O}\left(\delta r_{ii'}^2\right). \tag{34}$$

Boundary treatment

This study employs the boundary particle renormalization method to handle boundary conditions within the ISPH framework. Figure 3 illustrates the setup, including the dummy boundary particles, renormalization boundary particles, and the computation of the kernel renormalization factor (γ_a).

- **Dummy boundary particles:** These consist of a layer of boundary particles supplemented by two fictitious particles. The fictitious particles exert repulsive forces to minimize truncation errors in the smoothing function near the wall boundary. However, the use of dummy particles can lead to increased computational complexity in three-dimensional simulations due to the requirement for multiple particle layers.
- **Renormalization boundary particles:** This approach requires only a single boundary layer, significantly enhancing computational efficiency. The method calculates the kernel renormalization factor (γ_a) and its gradient ($\nabla\gamma_a$) at the boundary to implement the boundary conditions [47,52]. The Dirichlet conditions (e.g., fixed temperature and concentration) are straightforward to apply, while Neumann conditions (e.g., zero flux) are more challenging in complex geometries.

By adopting the renormalization approach, the study ensures accurate and computationally efficient boundary condition handling, suitable for the complex geometries involved in the cavity.

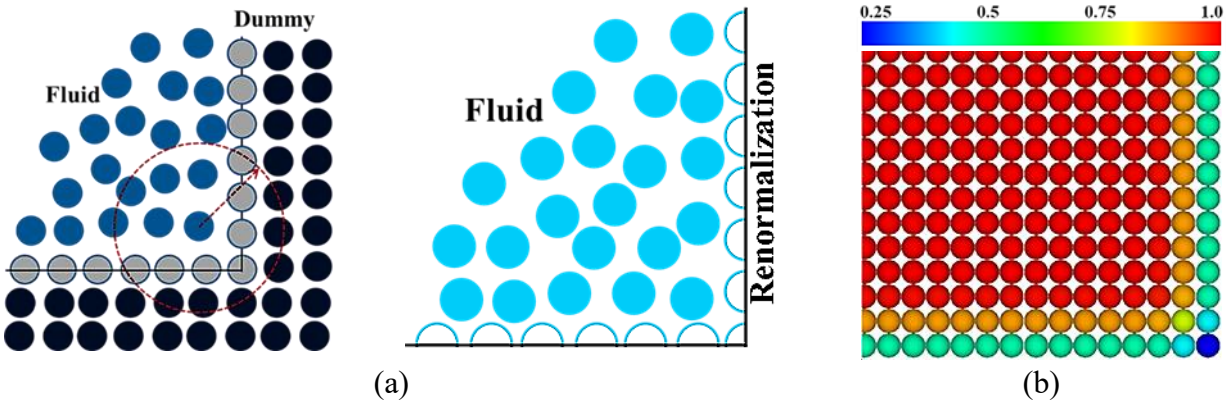

Figure 3. (a) Primary description of dummy boundary particles and renormalization boundary particles and (b) initial calculation of a kernel renormalization factor γ_a.

5. Validation tests

The validation section highlights the effectiveness and accuracy of the ISPH method by comparing its results with benchmark FEM simulations [57] and Davis's numerical data [58] across various Rayleigh numbers (Ra), demonstrating its robustness for natural convection scenarios. Figure 4 presents a comparative analysis between the current ISPH model and previously validated finite element method (FEM) results [57] for natural convection in a square cavity at various Rayleigh numbers ($Ra = 10^3, 10^4, 10^5, 10^6$). Figures 4(a)–4(c) depict vertical velocity at $X = 0.5$, horizontal velocity at $Y = 0.5$, and temperature profiles at $Y = 0.5$, respectively. The results indicate strong agreement between the ISPH and FEM models, with deviations primarily at higher Rayleigh numbers due to the increasing nonlinearity of natural convection. The velocity and temperature profiles show consistent trends across all Ra values, demonstrating the accuracy and reliability of the ISPH approach for capturing flow and thermal behaviors. These validations establish the robustness of the ISPH method in simulating natural convection and provide confidence in its application to complex configurations. Table 1 compares the average Nusselt numbers ($\overline{\mathrm{Nu}}$) obtained using the present ISPH model, the FEM method [57], and benchmark results from Davis [58] for natural convection in a square cavity across Rayleigh numbers (Ra) ranging from 10^3 to 10^6. The results show that the ISPH model closely aligns with both the FEM [57] and Davis benchmarks [58], with deviations becoming slightly more noticeable at higher Ra. These differences are attributed to the inherent approximations in numerical methods and the increased complexity of convection phenomena at higher Ra. The comparison demonstrates that the ISPH method provides reliable and accurate predictions, validating its effectiveness in modeling natural convection scenarios. Figure 5 illustrates the comparison of isotherm contour maps generated by the present ISPH method and the FEM [57] results at different Rayleigh numbers (Ra). Figures 5(a)–5(d) correspond to $Ra = 10^3$, $Ra = 10^4$, $Ra = 10^5$, and $Ra = 10^6$, respectively. The contours represent temperature distributions within the cavity, with values ranging from 0 to 1.0 at intervals of 0.1. The isotherms exhibit progressively steeper gradients and more pronounced curvature as Ra increases, indicating intensified convection. At lower Rayleigh numbers, the conduction-dominated regime produces smoother contours, while at higher Ra, convection becomes dominant, leading to more complex isotherm patterns. The close agreement

between the ISPH and FEM results across all cases demonstrates the reliability and accuracy of the ISPH method for modeling thermal behavior in natural convection scenarios.

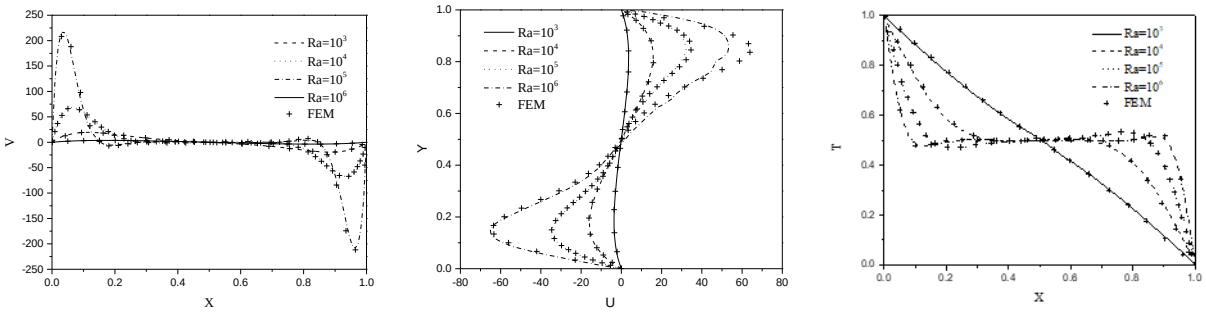

Figure 4. Comparison between (—) present ISPH method and (---) FEM results [57]. (a) Vertical velocity at $X = 0.5$, (b) horizontal velocity at $Y = 0.5$, and (c) temperature profile at $Y = 0.5$.

Table 1. Comparison of the current ISPH outcomes with Davis [58] and FEM simulations [57] for natural convection within a square cavity across different Rayleigh numbers (Ra).

$\overline{Nu}$	$Ra = 10^3$	$Ra = 10^4$	$Ra = 10^5$	$Ra = 10^6$
Davis [58]	1.118	2.243	4.519	8.798
FEM [57]	1.115	2.239	4.512	8.800
ISPH method	1.095	2.187	4.388	8.651

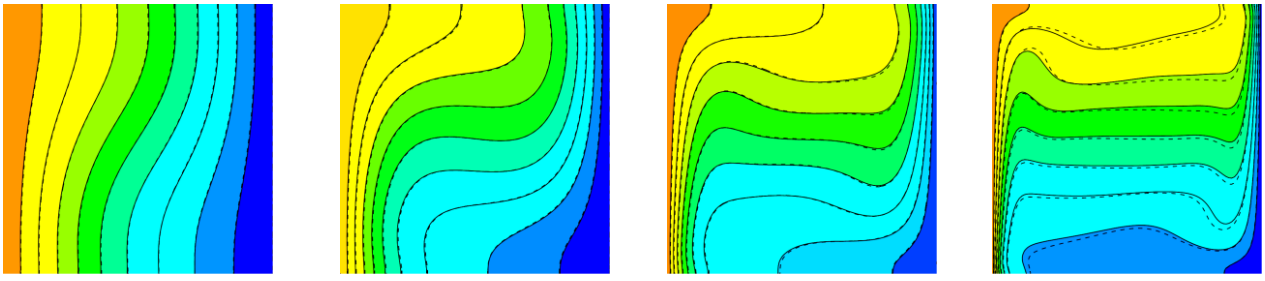

Figure 5. Comparison of isotherm contour maps: (—) present ISPH, (---) FEM [57]; (a) $Ra = 10^3$, (b) $Ra = 10^4$, (c) $Ra = 10^5$, (d) $Ra = 10^6$.

6. ANN modeling

An ANN model was developed to estimate $\overline{Nu}$ and $\overline{Sh}$ using an artificial intelligence-based approach. The model follows a multilayer perceptron (MLP) structure, a versatile neural network model known for its strong learning capabilities [59]. MLP networks consist of interconnected layers, with each layer directly connected to the next layer. There are basically three types of layers in an MLP

network: input, hidden, and output layers. Within this MLP framework, time (τ) and the Frank-Kamenetskii number (Fk) are used as input features, while the output layer generates the values of $\overline{Nu}$ and $\overline{Sh}$. The ANN architecture was based on an MLP with a single hidden layer. Determining the optimal number of neurons in the hidden layer posed a significant challenge, as no universally applicable method exists for this task [60]. To address this, an iterative approach was employed. Various configurations with different neuron counts were systematically tested, and their performance was evaluated based on metrics. Among these configurations, the model with 13 neurons in the hidden layer demonstrated the best overall performance, achieving a balance between accuracy and computational efficiency. Figure 6 displays the structure of the ANN model. The training process required careful organization of the dataset to ensure robust model generalization. A total of 56 data points were curated, following established methodologies in the literature [61]. These data points were divided into three subsets: 40 data points were allocated for training the model, 8 data points for validation, and 8 data points for testing. The training subset was used to optimize the model's weights and biases through backpropagation, while the validation subset served to monitor the model's performance during training and to prevent overfitting. Finally, the testing subset provided an independent evaluation of the model's predictive capability. The training process employed the Levenberg–Marquardt algorithm, a widely used optimization method in ANN applications due to its efficiency in handling nonlinear optimization problems. The activation function used in the hidden layer was the hyperbolic tangent sigmoid (tansig) function, which facilitates learning complex nonlinear relationships, while the output layer utilized a linear activation function to accommodate the continuous output variables. The equations for these transfer functions are:

$$f(x) = \frac{1}{1+exp\,(-x)} \tag{35}$$

$$purelin(x) = x. \tag{36}$$

The training process was terminated when the validation error failed to improve for a predetermined number of epochs (early stopping criterion), thereby minimizing the risk of overfitting. This detailed procedure ensured that the ANN model was appropriately configured, trained, and validated to achieve an accurate solution to the governing equations while maintaining computational efficiency. To assess the model's performance, several standard metrics were used, including mean squared error (MSE), coefficient of determination (R), and margin of deviation (MoD). The formulas for these metrics, essential in evaluating model accuracy, are provided below [60]:

$$MSE = \frac{1}{N}\sum_{i=1}^{N}(X_{targ\,(i)} - X_{pred(i)})^2 \tag{37}$$

$$R = \sqrt{1 - \frac{\sum_{i=1}^{N}(X_{targ(i)} - X_{pred(i)})^2}{\sum_{i=1}^{N}(X_{targ(i)})^2}} \tag{38}$$

$$MoD\ (\%) = \left[\frac{X_{targ} - X_{pred}}{X_{targ}}\right] x\ 100 \tag{39}$$

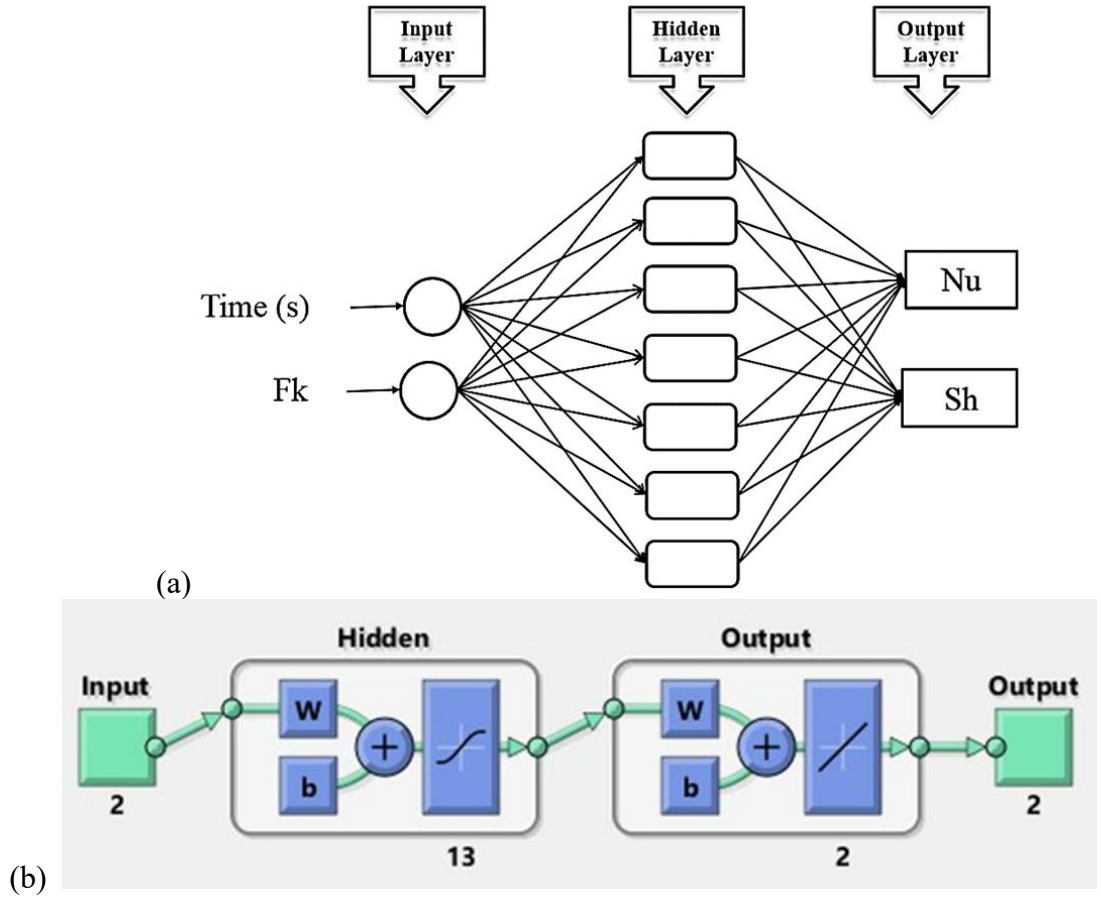

Figure 6. ANN model. (a) Configuration architecture. (b) Principal structure.

The ANN model's training performance was evaluated for its robustness and reliability. The dataset was designed to capture a wide range of parametric variations in a problem. The model's predictive accuracy and generalization ability were assessed using a comparison between predicted and target values. The results showed high prediction accuracy, minimal residual errors, and strong correlation between predicted and target values. The consistency of the model's performance across validation and testing subsets confirmed its security and diversity, demonstrating the model's representativeness and dependability.

7. Results and discussion

This study performed numerical simulations to analyze the impact of exothermic chemical reactions, magnetic fields, and the Cattaneo–Christov heat flux on double diffusion within a nanofluid-filled cavity with a rotating Z-shaped fin. The following ranges for the controlling parameters were considered: Frank-Kamenetskii number (Fk): $0 \le Fk \le 6$; Cattaneo–Christov heat flux coefficient (δ_c): $0 \le \delta_c \le 0.001$; Hartmann number (Ha): $0 \le Ha \le 50$; Soret number (Sr): $0 \le Sr \le 2$; Dufour number (Du): $0 \le Du \le 2$; nanoparticle volume fraction (ϕ): $0 \le \phi \le 0.15$; and Z-shaped fin height from 0.5 to 0.6 m, width from 0.4 to 0.7 m, and length from 0.3 to 0.8 m. Fixed parameters included $\delta_c = 0.0001$, Rayleigh number ($Ra = 10^4$), $S_r = 1.2$, $Du = 0.6$, $\phi = 0.05$, fin orientation angle ($\gamma = 45°$), $F_k = 2$, $N = 2$, and $H_a = 10$. Figures 7–9 depict temperature contours (θ), concentration contours (Φ), and the velocity field (V) under varying F_k values across time

intervals $\tau = 0.01,\ 0.1$, and 0.3. When F_k increases, heat transfer intensifies, expanding thermal contours over time (τ). At $\tau = 0.01$, the cooling region covers much of the cavity, with hot areas along the vertical walls. As time progresses, the isotherms spread upward. Figure 8 shows that concentration (Φ) shifts slightly as F_k increases, while rotation of the Z-shaped fin at $\tau = 0.3$ causes Φ to spread from top to bottom. In Figure 9, higher F_k values enhance the maximum velocity field. Figure 10 illustrates how varying the Hartmann number (Ha) affects θ, Φ, and V, with Lorentz forces from a larger Ha value slowing fluid velocity. When Ha rises from 0 to 50, maximum velocity drops by 61.99%. Higher Ha values also narrow the temperature and concentration distributions. Figure 11 shows the variations in the average Nusselt number $(\overline{Nu})$ and average Sherwood number $(\overline{Sh})$ over dimensionless time (τ) under different Hartmann numbers (Ha), demonstrating the influence of magnetic fields on heat and mass transfer. At $Ha = 0$, where no magnetic field is present, $\overline{Nu}$ and $\overline{Sh}$ are highest due to enhanced convection. As Ha increases to 20 and 50, the Lorentz force suppresses fluid motion, leading to reduced convective heat and mass transfer, as reflected in the decreasing $\overline{Nu}$ and $\overline{Sh}$ values. These results highlight the magnetic field's ability to regulate convection, which has significant applications in industries such as magnetic cooling, MHD pumps, and thermal management systems. The ability to control Ha offers practical solutions for optimizing processes that require precise heat and mass transfer control, such as preventing overheating or improving chemical reactor efficiency. The observed suppression of convection with increasing Hartmann number (Ha) demonstrates its applicability in magnetic cooling systems and MHD pumps, where precise thermal regulation is critical. Figure 12 assesses Dufour number (Du) effects on θ, Φ, and V. Results suggest that Du, which relates mass gradients to energy flux, has minimal impact on temperature, concentration, and velocity fields, likely due to the cooling fin's presence. $\overline{Nu}$ and $\overline{Sh}$ remained largely unaffected by Du variations. Figure 13 examines how temperature, concentration, and velocity fields respond to increases in nanoparticle volume fraction (ϕ), representing the percentage of solid particles within the nanofluid mixture. Higher ϕ values extend the cooling region and raise fluid viscosity, reducing velocity. When ϕ increases from 0 to 0.15, maximum velocity decreases by 19.71% due to increased viscosity. Figure 14 indicates that as ϕ grows from 0 to 0.15, $\overline{Nu}$ increases by 22.43%, and $\overline{Sh}$ increases by 116.3%. The enhancement in $\overline{Nu}$ and $\overline{Sh}$ with increasing nanoparticle volume fraction (ϕ) highlights its potential for optimizing heat exchangers and nanofluid-based solar collectors. Figures 15 and 16 analyze the Cattaneo–Christov heat flux (δ_c) effects on θ and V across times $\tau = 0.01,\ 0.1$, and 0.3, showing mild changes in temperature fields and a slight velocity rise with increasing δ_c. Figures 17 and 18 explore the influence of Soret number (Sr) on θ, Φ, and V, and on $\overline{Nu}$ and $\overline{Sh}$. As Sr increases, thermal gradients cause lighter particles to move toward warmer areas and heavier particles toward cooler zones. Figure 17 shows that higher Sr slightly modifies the isotherms and significantly enhances concentration. With Sr increasing from 0 to 2, maximum velocity accelerates by 130.27%. Figures 19 and 20 explore how altering Z-shaped fin length affects θ, Φ, V, and $\overline{Nu}$ and $\overline{Sh}$. Reducing the fin's length strengthens temperature and concentration distributions within the cavity, raising maximum velocity by 16.99%. The Z-shaped fin's presence, despite slow rotation, acts as a flow barrier, highlighting the importance of optimal fin sizing for industrial cooling. Figure 20 shows that reducing fin size results in decreases in $\overline{Nu}$ and $\overline{Sh}$, underscoring the fin's role in regulating heat and mass transfer and fluid velocity within the cavity.

The training process of the ANN model was thoroughly evaluated using performance metrics and visual aids for better understanding and clarity. Figure 21 illustrates the training performance graph, which tracks the variation of the MSE over successive training epochs. The graph clearly demonstrates a consistent decline in MSE values, starting from an initially high value and converging toward

minimal error levels as the training progressed. The convergence indicates effective learning and optimization of the ANN model. For clarity, annotations in Figure 21 highlight key stages in the training process, such as the initialization phase with high errors, the rapid error reduction phase, and the stabilization of error levels as the model approaches optimal performance. These annotations provide insight into the dynamics of the training process, aiding readers in interpreting the graph more effectively. Figure 22 provides additional validation of the model's training through an error histogram, which visualizes the distribution of prediction errors across the dataset. The error values are concentrated near zero, confirming that the model achieves a high degree of accuracy and minimal residuals. Following training verification, Figure 23 compares ANN-predicted and target $\overline{Nu}$ and $\overline{Sh}$ values, with close alignment seen. Figure 24 presents MoD values, which largely remain near zero, signifying minimal prediction error. Mean deviation rates for $\overline{Nu}$ and $\overline{Sh}$ are 0.01% and 0.06%, respectively. In Figure 25, differences between target and ANN values further support model precision. Figure 26 plots target values (x-axis) against ANN predictions (y-axis), showing alignment along the zero-error line for both outputs. The ANN model's MSE was 4.21×10^{-6} and R value was 0.99994, confirming high prediction accuracy for $\overline{Nu}$ and $\overline{Sh}$.

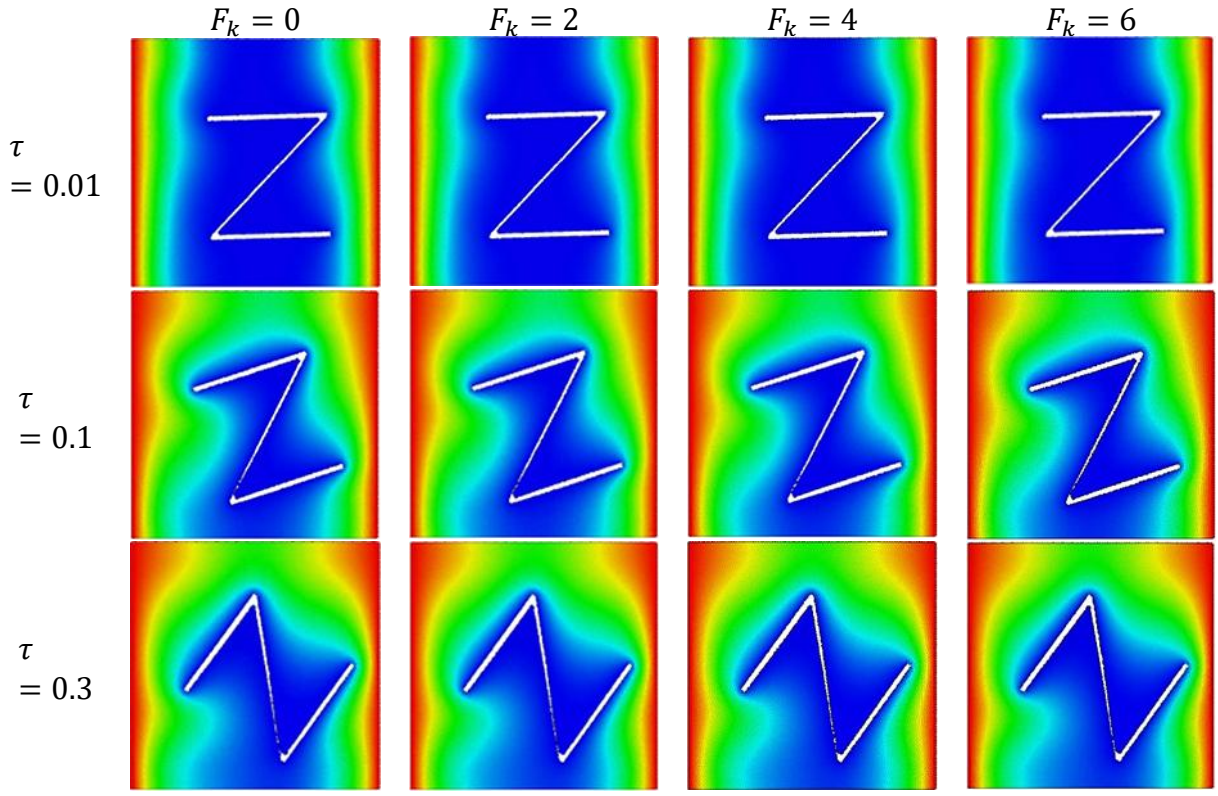

Figure 7. Isotherms θ under the variation of Frank-Kamenetskii number F_k at different time instances $\tau = 0.01, 01$, and 0.3.

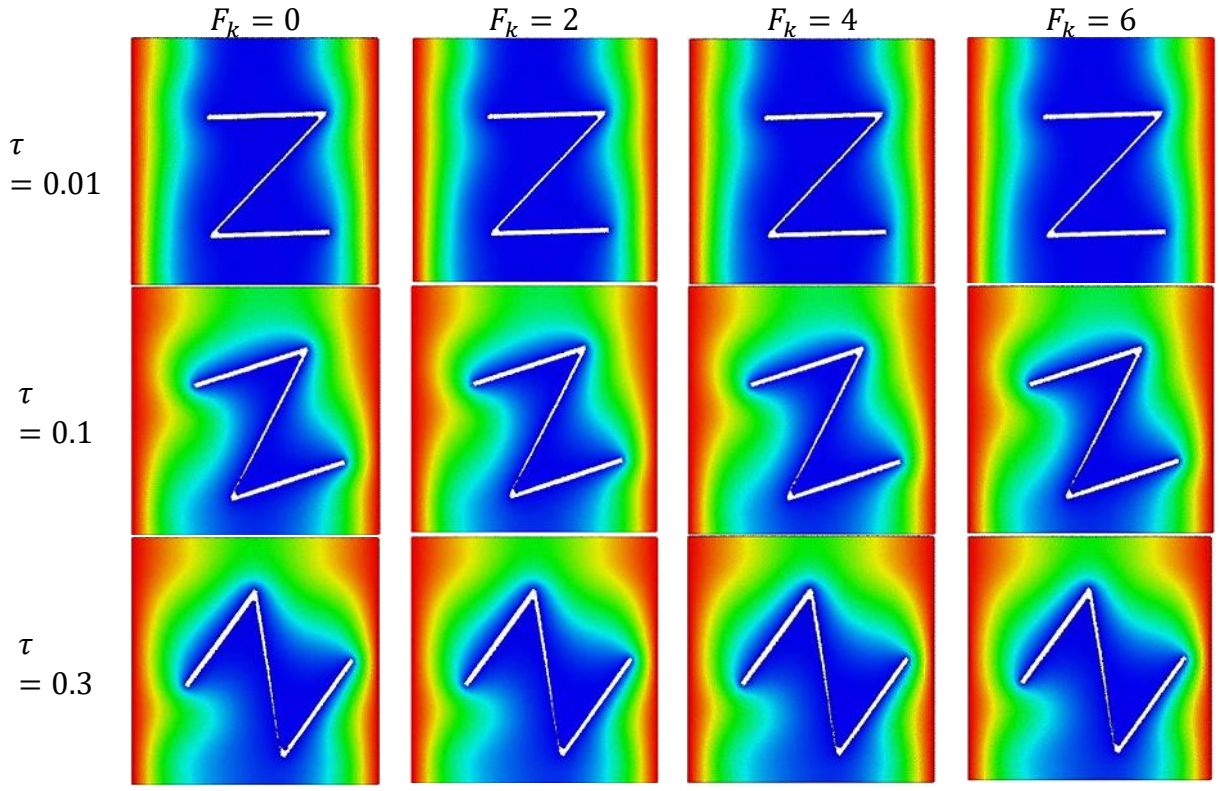

Figure 8. Isoconcentration Φ under the variation of Frank-Kamenetskii number F_k at different time instances $\tau = 0.01, 01$, and 0.3.

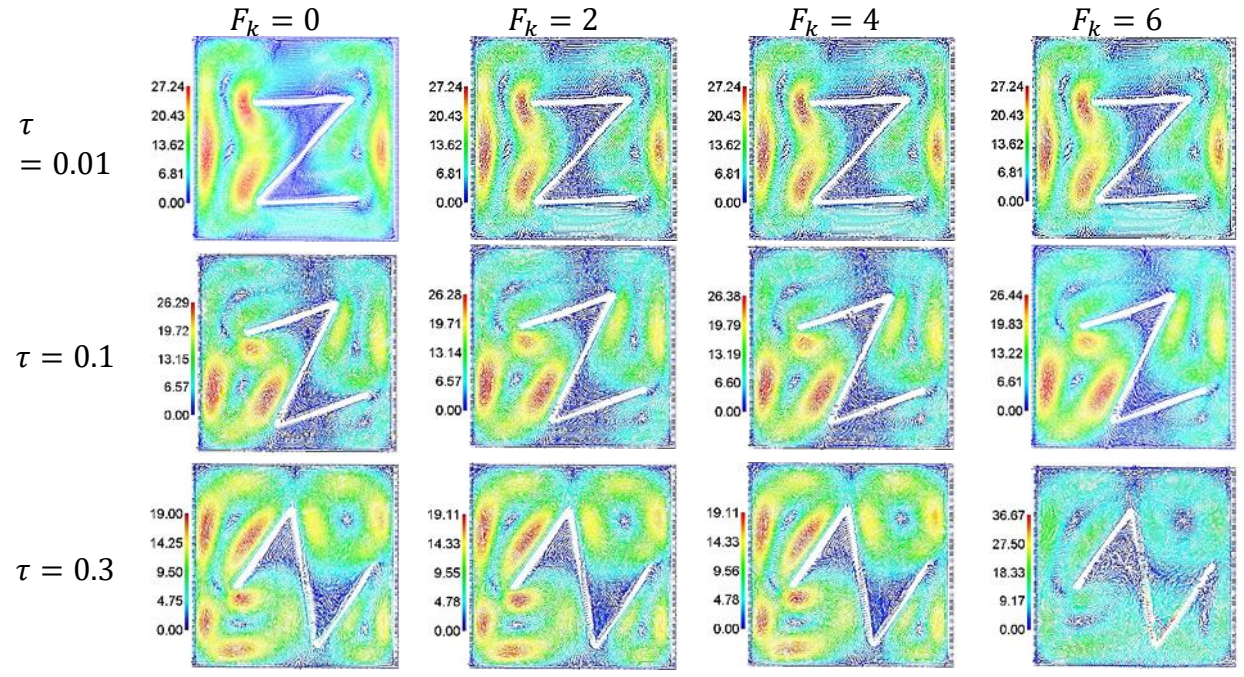

Figure 9. Velocity field $\boldsymbol{V}$ under the variation of Frank-Kamenetskii number F_k at different time instances $\tau = 0.01, 01$, and 0.3.

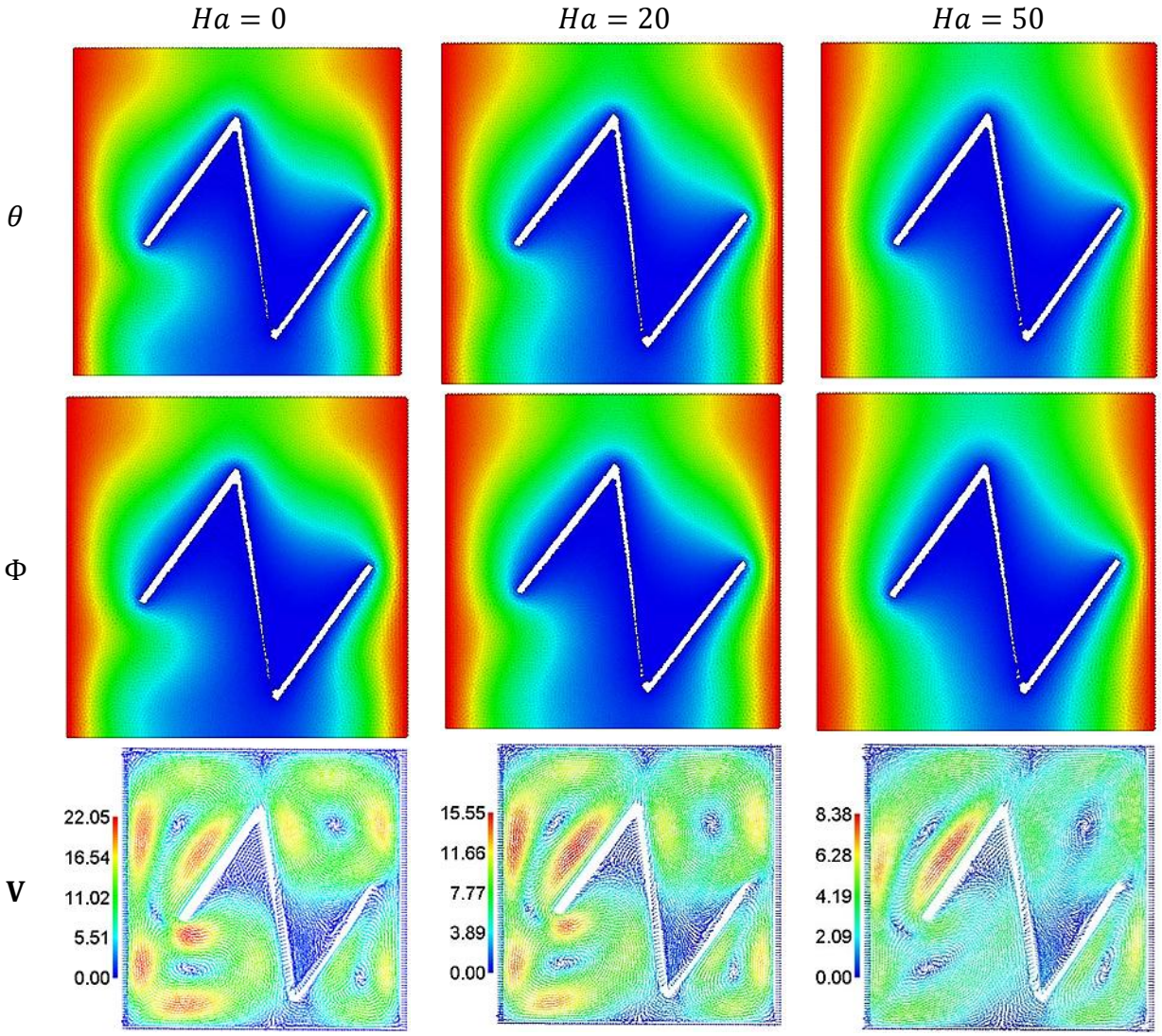

Figure 10. Distributions of θ, Φ, and $\boldsymbol{V}$ under variations of Hartmann number Ha.

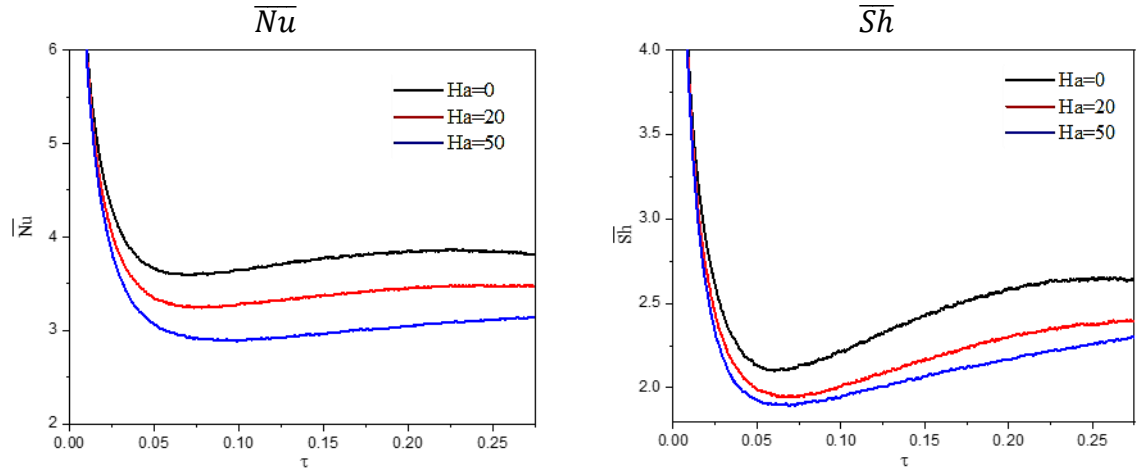

Figure 11. Average $\overline{Nu}$ and $\overline{Sh}$ under variations of Hartmann number Ha.

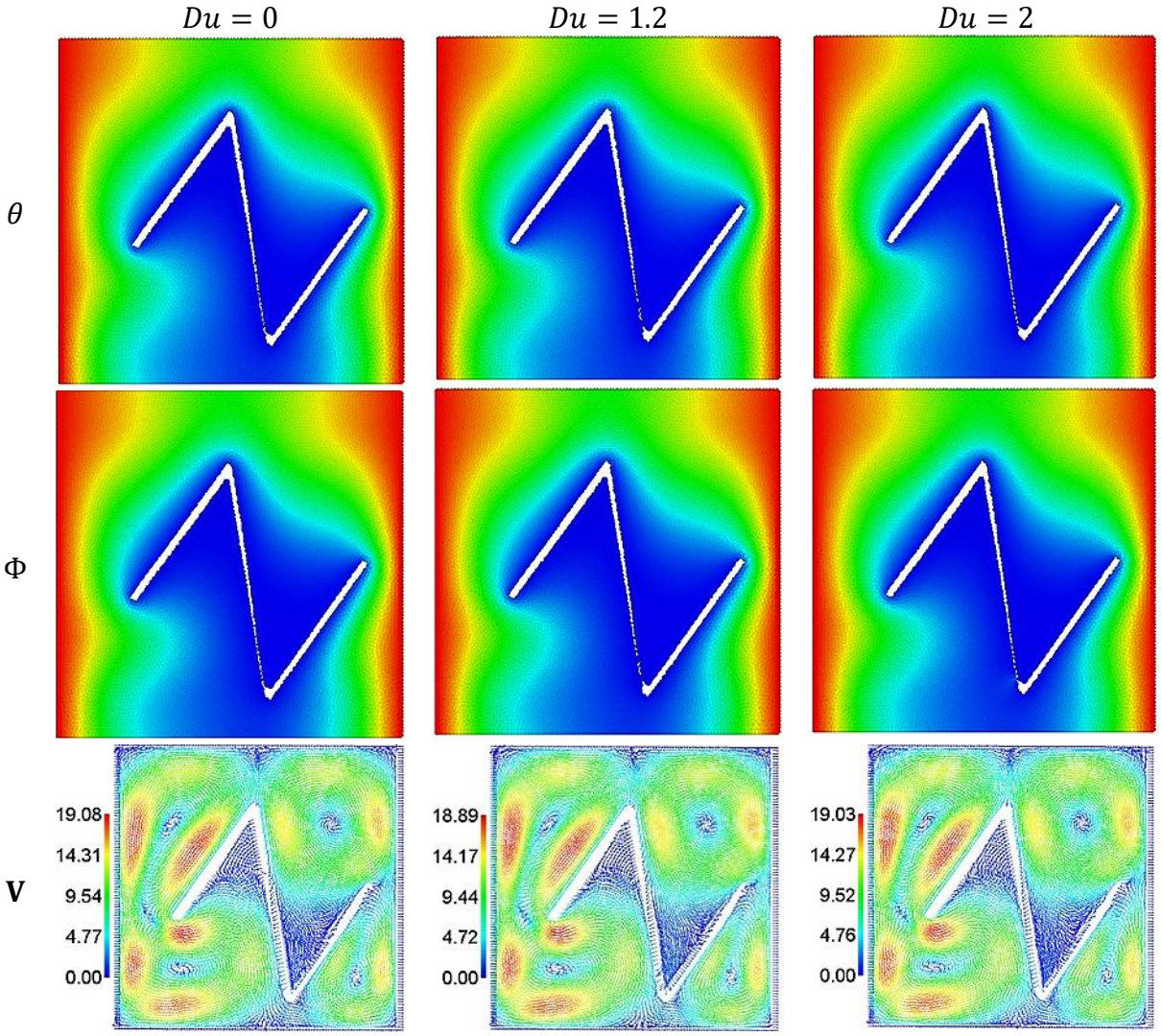

Figure 12. Distributions of θ, Φ, and $\boldsymbol{V}$ under variations of Dufour number Du.

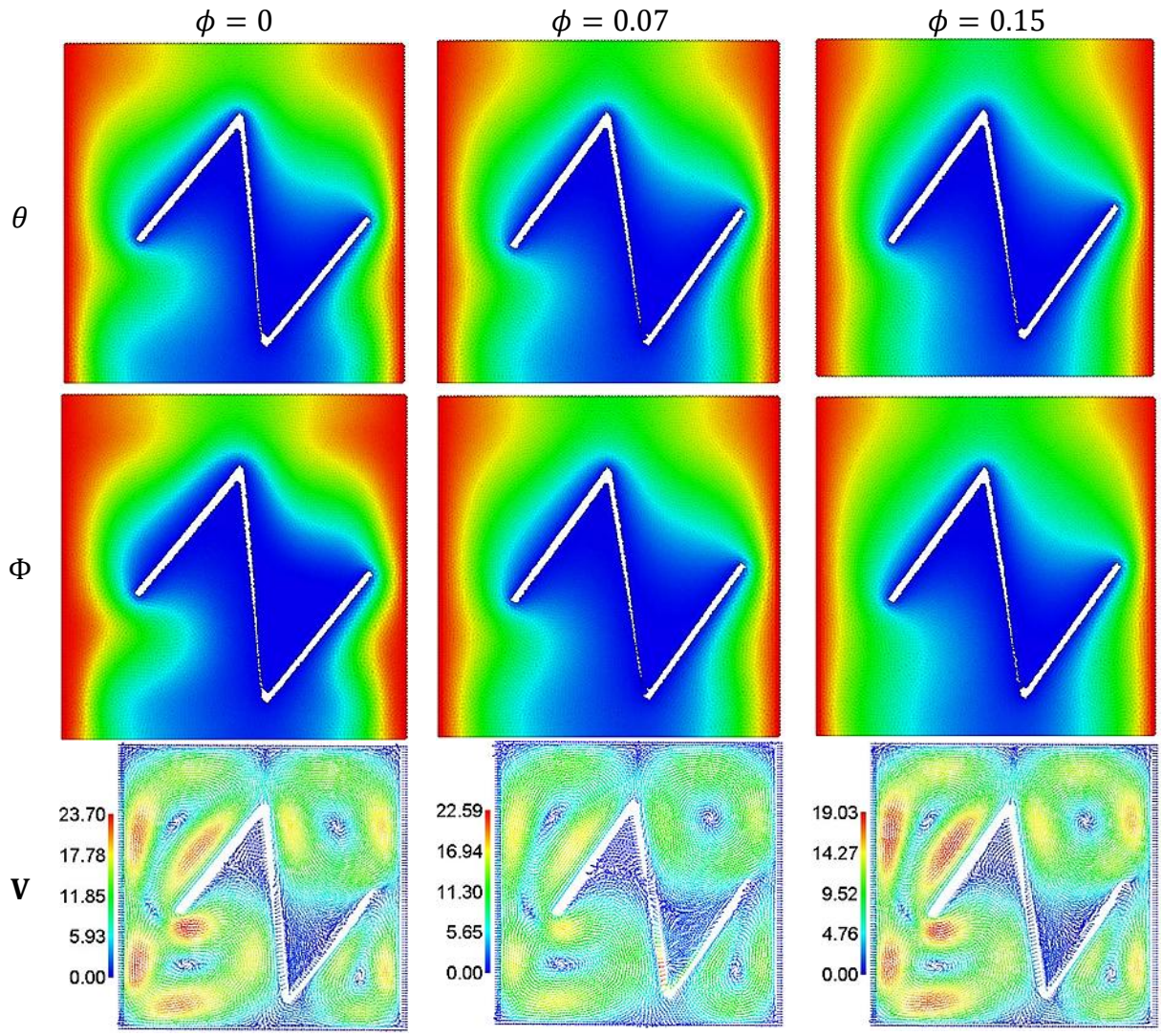

Figure 13. Distributions of θ, Φ, and $\boldsymbol{V}$ under variations of solid volume fraction ϕ.

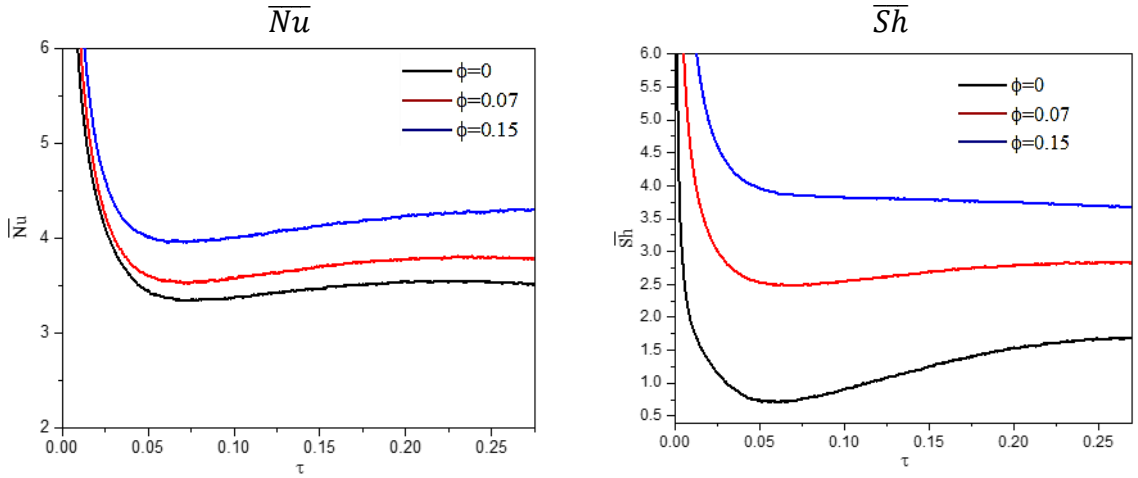

Figure 14. Average $\overline{Nu}$ and $\overline{Sh}$ under variations of solid volume fraction ϕ.

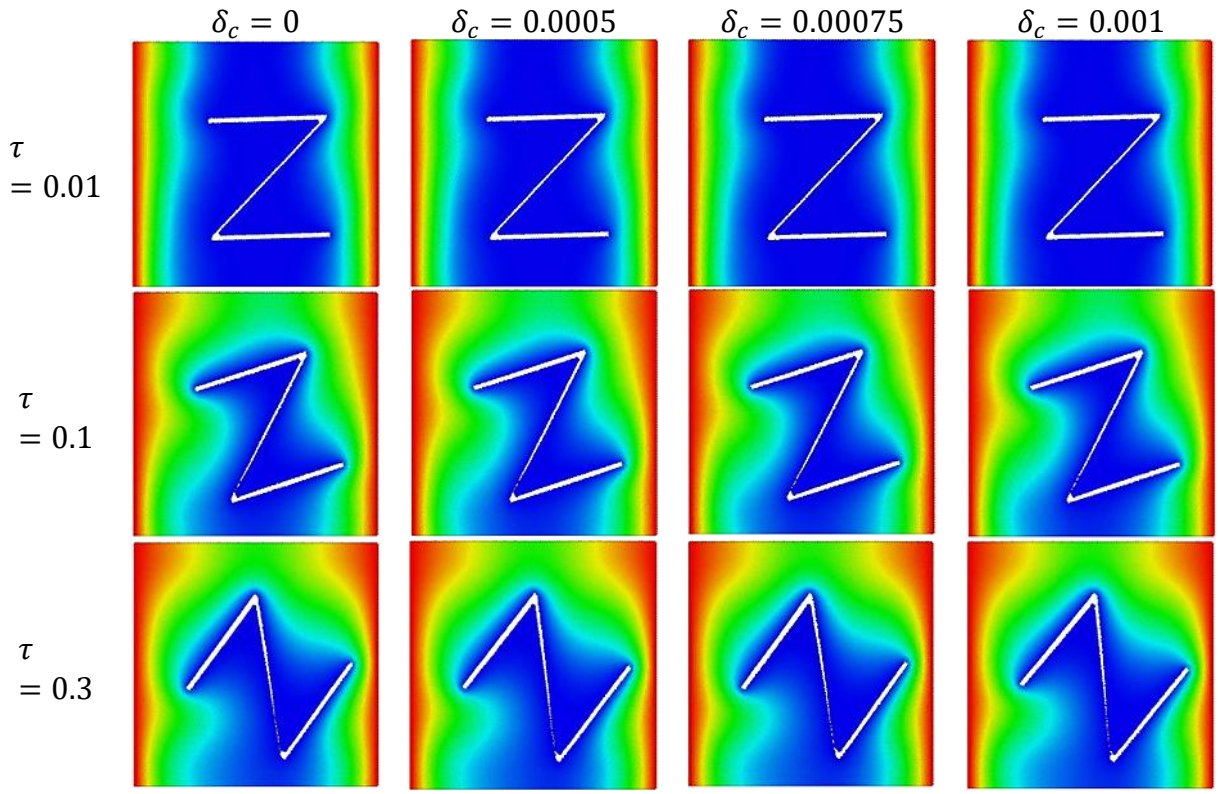

Figure 15. Isotherms θ under variation of the Cattaneo–Christov heat flux parameter δ_c at different time instances $\tau = 0.01, 01$, and 0.3.

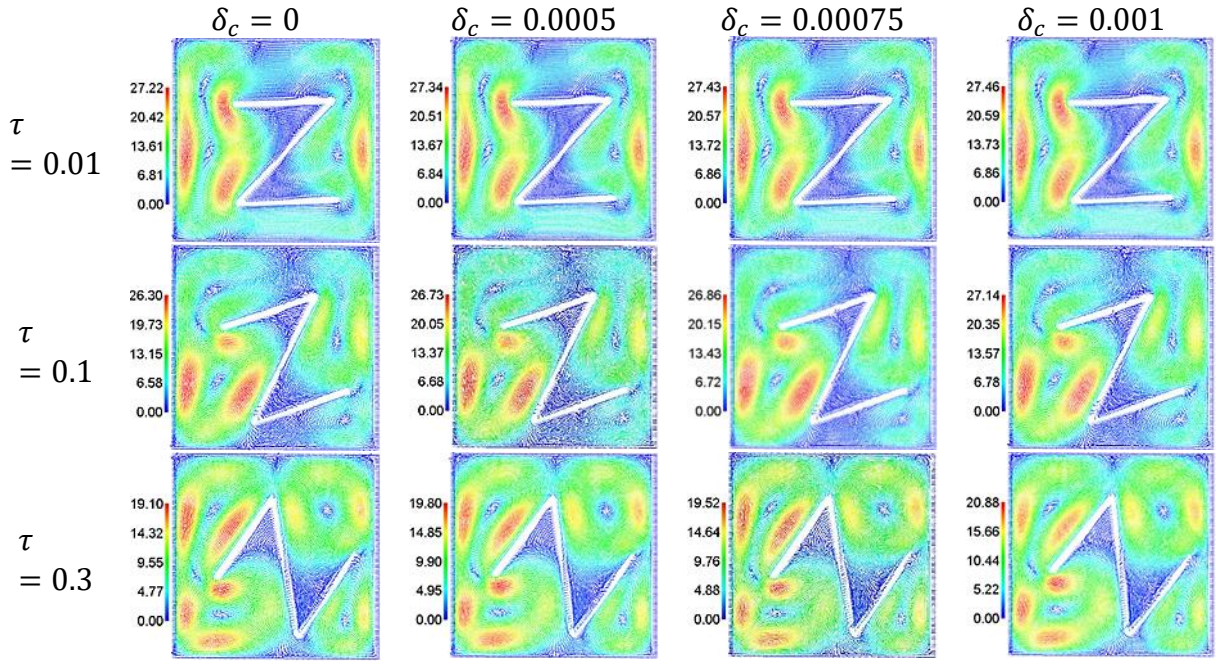

Figure 16. Velocity field $\boldsymbol{V}$ under variation of the Cattaneo–Christov heat flux parameter δ_c at different time instances $\tau = 0.01, 01$, and 0.3.

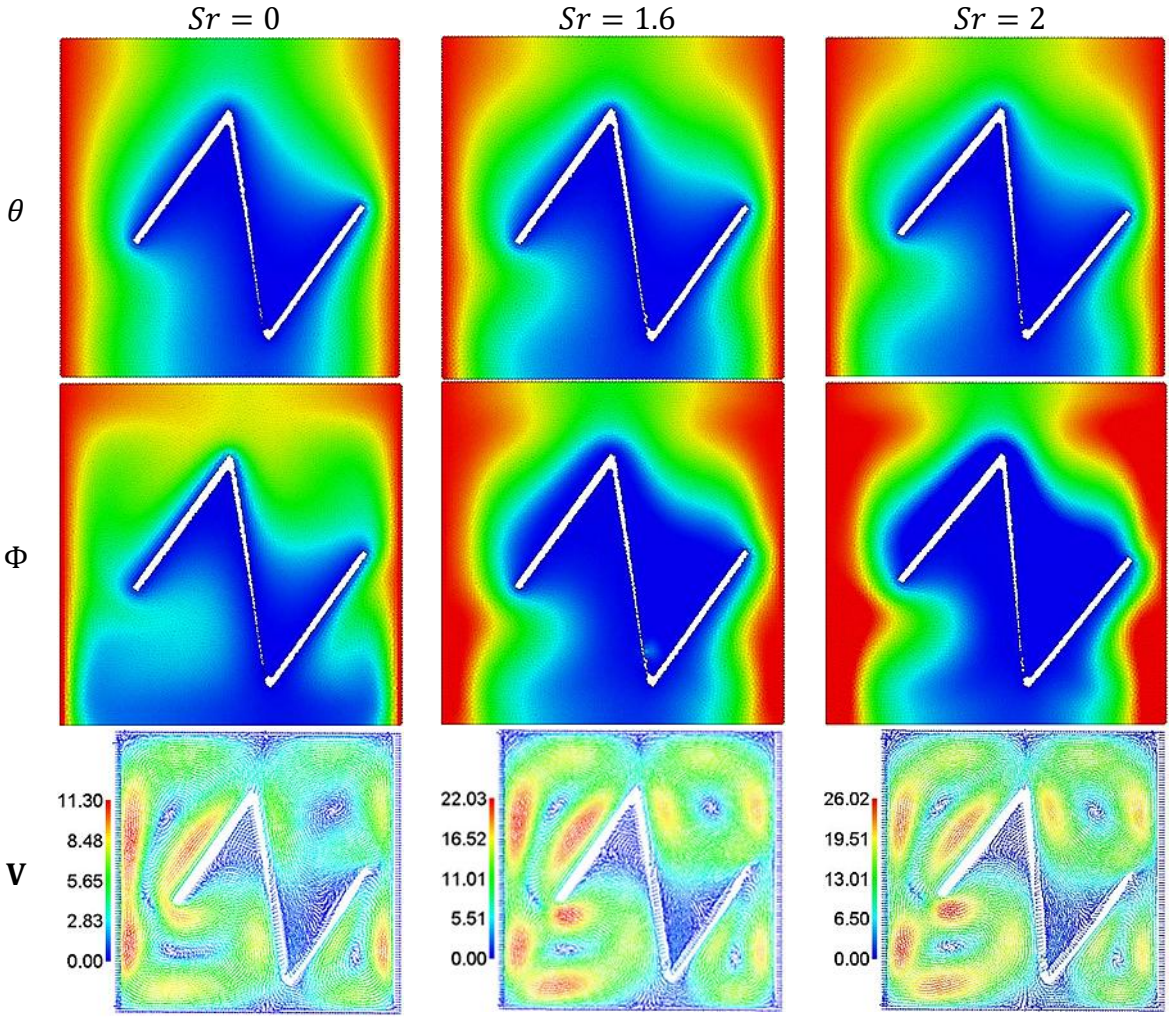

Figure 17. Distributions of θ, Φ, and $\boldsymbol{V}$ under variations of Soret number Sr.

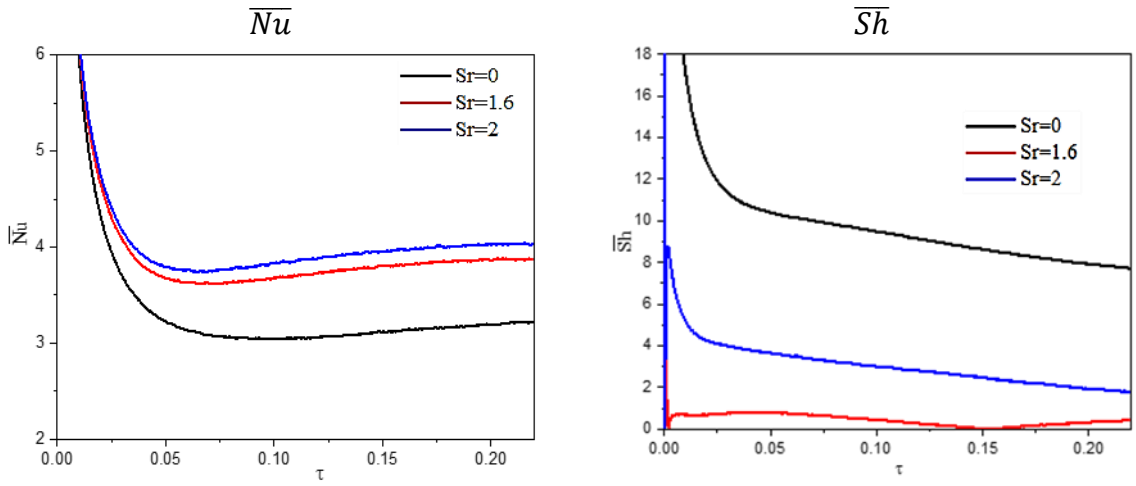

Figure 18. Average $\overline{Nu}$ and $\overline{Sh}$ under variations of Soret number Sr.

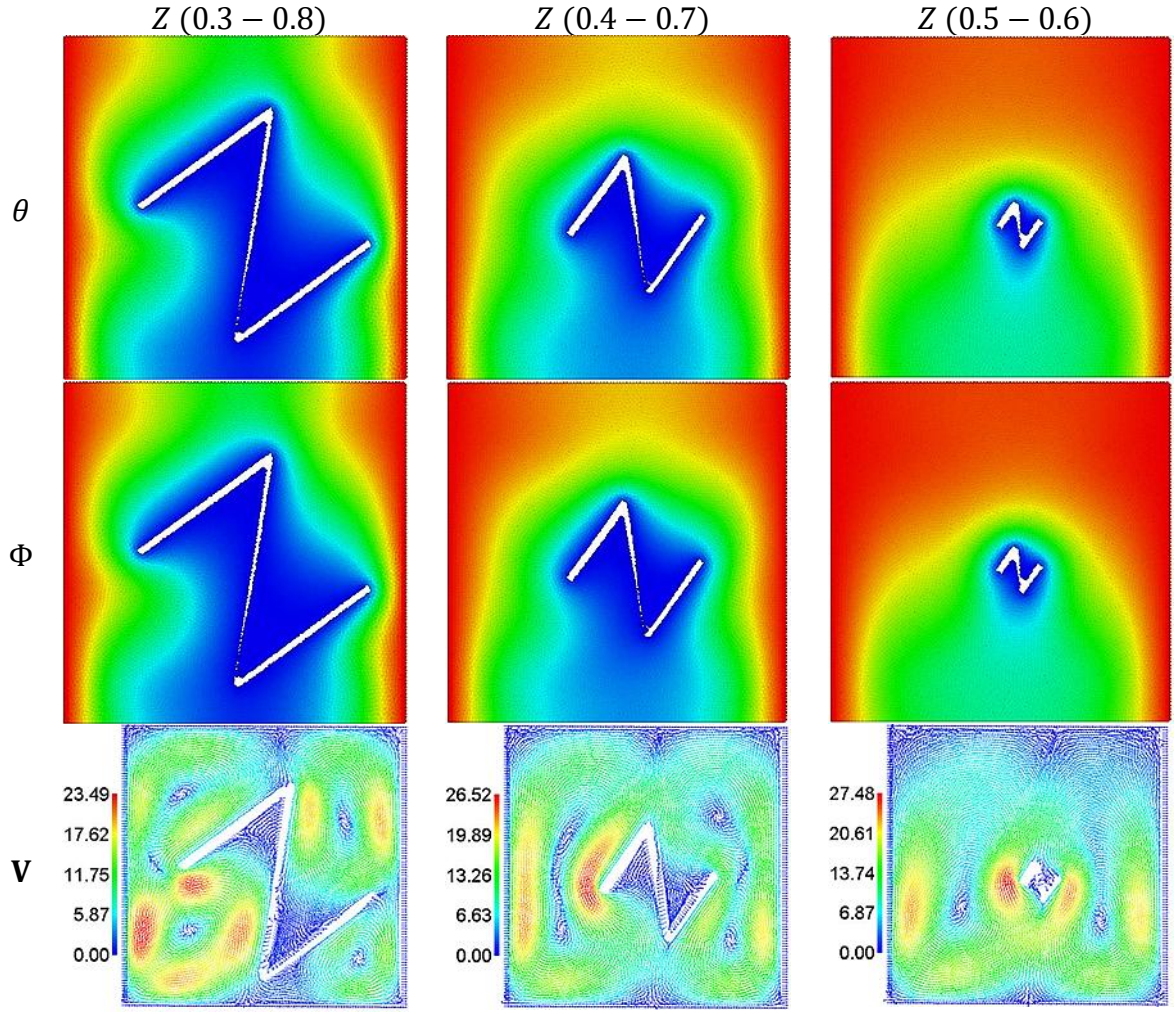

Figure 19. Distributions of θ, Φ, and $\boldsymbol{V}$ under variations of Z-shaped length.

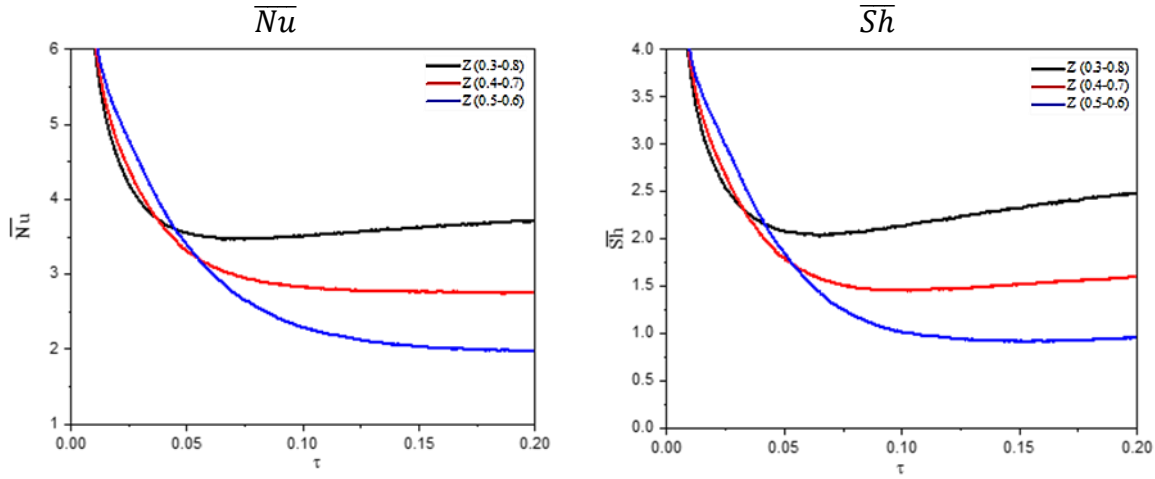

Figure 20. Average $\overline{Nu}$ and $\overline{Sh}$ under variations of Z-shaped length.

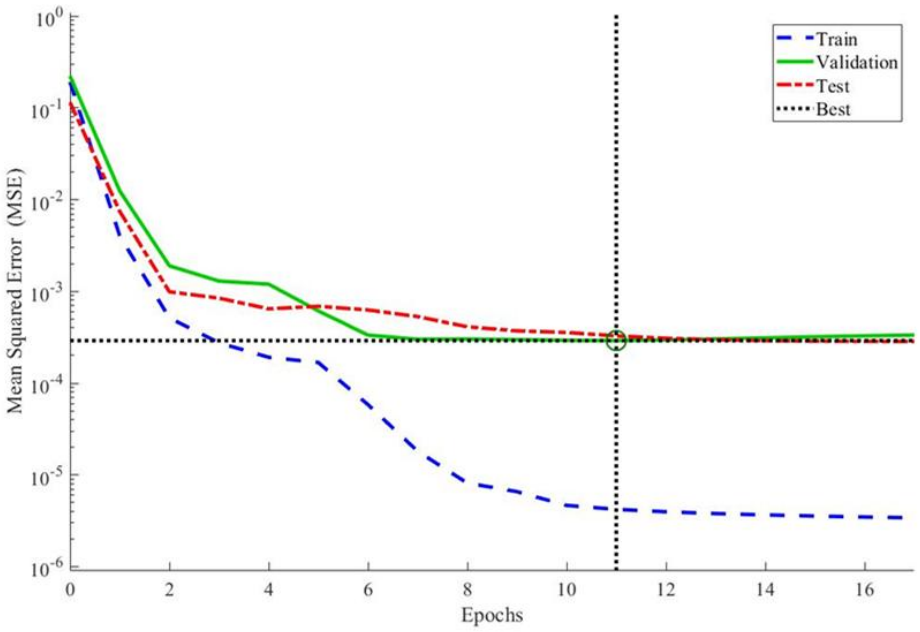

Figure 21. Training performance graph of the ANN model.

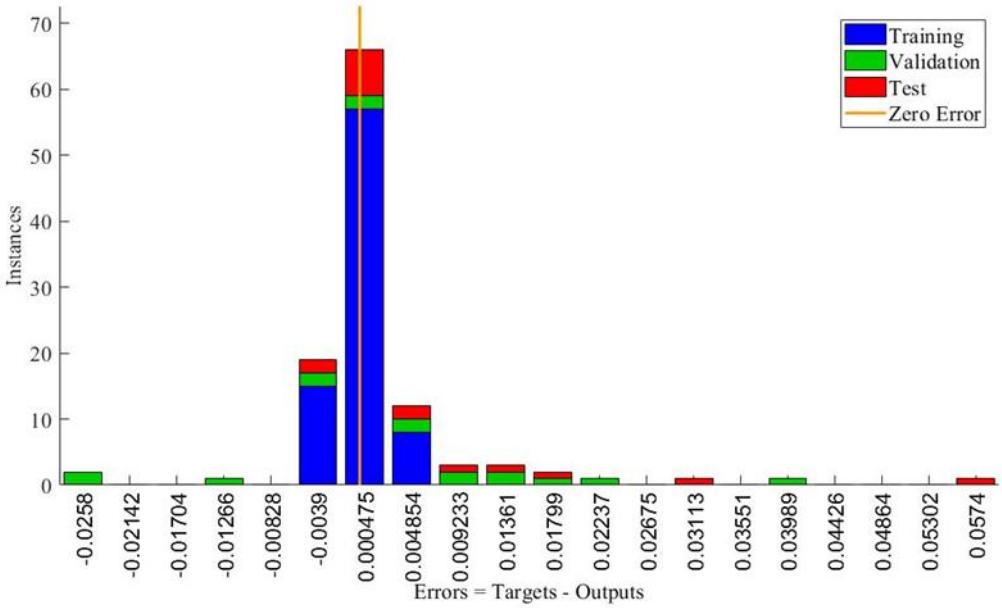

Figure 22. Error histogram of the ANN model.

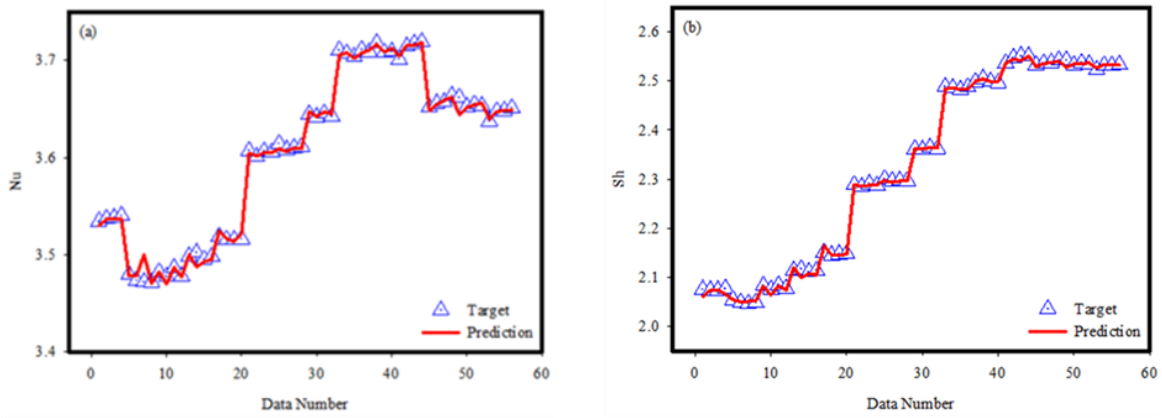

Figure 23. Target values for each data point with the data obtained from the ANN model.

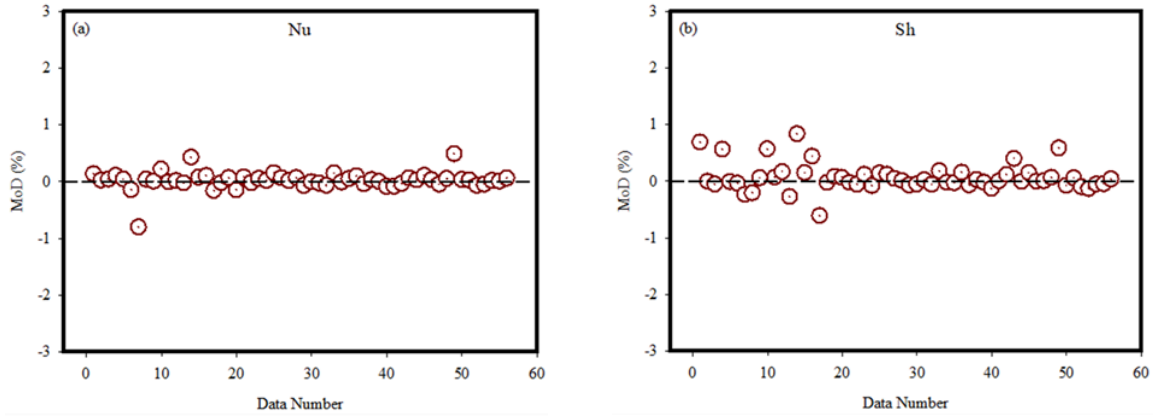

Figure 24. MoD values according to data number.

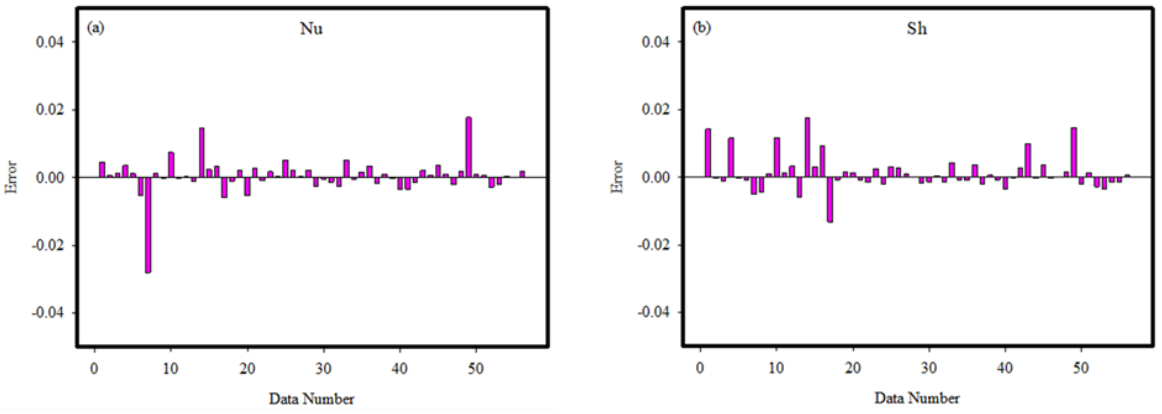

Figure 25. MoD values according to data number.

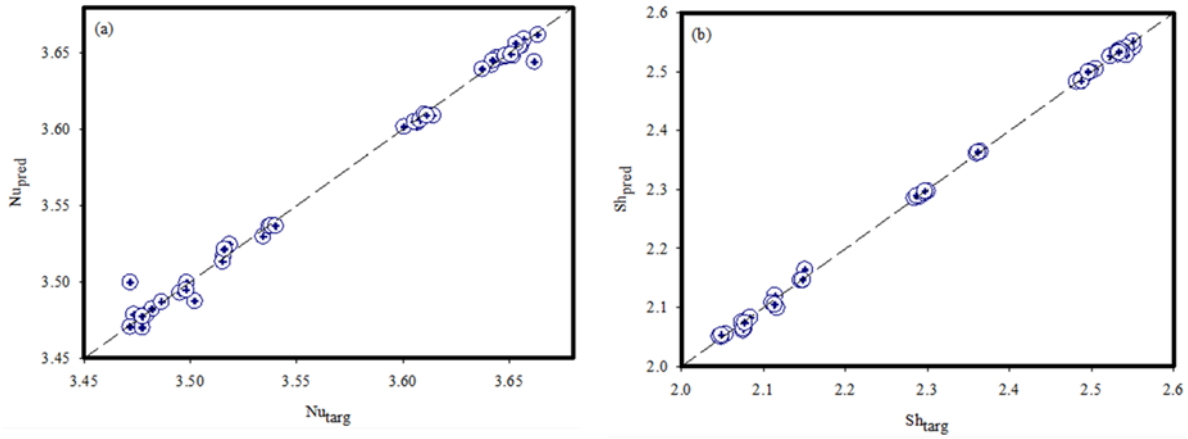

Figure 26. Target and prediction values.

8. Conclusions

This study employed numerical simulations to investigate the effects of exothermic chemical reactions, magnetic fields, and Cattaneo–Christov heat flux on thermal and solutal transport within a nanofluid-filled square cavity containing a rotating Z-shaped fin. The ISPH approach facilitated the analysis of fluid-structure interactions between the rotating fin and nanofluid, providing insights applicable to cooling, energy, and heat exchange systems. The study revealed that increasing the Frank-Kamenetskii number significantly enhances convection, improving thermal and concentration transfer and velocity. Magnetic field–induced Lorentz forces were shown to suppress fluid motion, reducing velocity by 61.99% and leading to decreases in average Nusselt and Sherwood numbers by 16.87% and 11.81%, respectively. Increasing the nanoparticle volume fraction to 15% raised the average Nusselt number by 22.43% and the Sherwood number by 116.3%, despite slowing fluid velocity by 19.71% due to increased viscosity. The Soret effect significantly improved concentration and velocity fields, while fin geometry was found to play a critical role in optimizing heat and mass transfer. The integration of an ANN model demonstrated high accuracy in predicting average Nusselt and Sherwood numbers, making it an effective tool for evaluating nanofluid performance. This work advances the understanding of heat exchange in nanofluids by providing a detailed analysis of the combined effects of magnetic fields, exothermic reactions, and nanoparticle concentration. The novelty lies in the integrated ISPH-ANN framework, which efficiently models complex thermal and solutal interactions, enabling accurate predictions for practical applications such as thermal management systems, energy storage devices, and industrial cooling processes. These findings offer valuable guidance for designing and optimizing advanced heat exchange technologies in various industrial settings. Future work could explore extending the model to three-dimensional systems, considering non-Newtonian nanofluids, or incorporating transient effects of dynamic fin motion. Additionally, experimental validation and application of the ISPH-ANN framework to practical systems, such as solar collectors, desalination units, and heat exchangers, would provide deeper insights and further generalize the findings.

Limitations of the study

This study assumes incompressible, laminar, and two-dimensional flow using the Boussinesq approximation and constant nanofluid properties, which may not fully capture real-world complexities such as three-dimensional effects or variable properties. The boundary conditions, including adiabatic and impermeable walls, simplify practical scenarios. The results are specific to the chosen geometry and parameter ranges, limiting generalizability to other configurations. Additionally, the Z-shaped fin is modeled as a rigid body with fixed rotational speed, excluding potential effects of deformation or variable speeds. Finally, computational constraints, such as resolution and the efficiency of the ISPH method, may restrict the precision of the simulations. These limitations highlight areas for future research to enhance the model's applicability and accuracy.

Author contributions

Kuiyu Cheng and Abdelraheem M. Aly conceptualized the study, while Abdelraheem M. Aly, Nghia Nguyen Ho, and Andaç Batur Çolak handled methodology and software. Validation and formal analysis were conducted by Sang-Wook Lee and Weaam Alhejaili. Kuiyu Cheng, Nghia Nguyen Ho, and Andaç Batur Çolak managed data curation, with all authors contributing to writing, review, and editing. Abdelraheem M. Aly and Sang-Wook Lee supervised the work, and project administration and funding were managed by Sang-Wook Lee and Weaam Alhejaili. All authors approved the final manuscript.

Use of Generative-AI tools declaration

The authors declare they have not used Artificial Intelligence (AI) tools in the creation of this article.

Acknowledgments

The first author (A.M. Aly) extends his appreciation to the Deanship of Scientific Research at King Khalid University, Abha, Saudi Arabia, for funding this work through the Research Group Project under Grant Number (RGP. 2/613/45). This research was funded by the Princess Nourah bint Abdulrahman University Researchers Supporting Project number (PNURSP2025R229), Princess Nourah bint Abdulrahman University, Riyadh, Saudi Arabia. This work was supported by Regional Innovation Cluster Development (R&D) by the Ministry of Trade, Industry and Energy (MOTIE, Korea) [Project Name: Open Innovation Project for Convergence Industry of Battery/Fuel Cell for Mobility Electrification and Energy Production/Storage (P0025406).

Conflict of interest

The authors declare that they have no conflict of interest.

References

1. S. M. Saeidi, J. M. Khodadadi, Forced convection in a square cavity with inlet and outlet ports, *Int. J. Heat Mass Tran.*, **49** (2006), 1896−1906. https://doi.org/10.1016/j.ijheatmasstransfer.2005.10.033

2. M. A. Ismael, H. F. Jasim, Role of the fluid-structure interaction in mixed convection in a vented cavity, *Int. J. Mech. Sci.*, **135** (2018), 190−202. https://doi.org/10.1016/j.ijmecsci.2017.11.001
3. S. U. Choi, J. A. Eastman, *Enhancing thermal conductivity of fluids with nanoparticles*, Argonne National Lab.(ANL), Argonne, IL (United States), 1995.
4. S. K. Das, S. U. Choi, W. Yu, T. Pradeep, *Nanofluids: Science and technology*, John Wiley & Sons, 2007.
5. Y. Yang, Z. G. Zhang, E. A. Grulke, W. B. Anderson, G. Wu, Heat transfer properties of nanoparticle-in-fluid dispersions (nanofluids) in laminar flow, *Int. J. Heat Mass Tran.*, **48** (2005), 1107−1116. https://doi.org/10.1016/j.ijheatmasstransfer.2004.09.038
6. N. Putra, F. N. Iskandar, Application of nanofluids to a heat pipe liquid-block and the thermoelectric cooling of electronic equipment, *Exp. Therm. Fluid Sci.*, **35** (2011), 1274−1281. https://doi.org/10.1016/j.expthermflusci.2011.04.015
7. O. Mahian, A. Kianifar, S. A. Kalogirou, I. Pop, S. Wongwises, A review of the applications of nanofluids in solar energy, *Int. J. Heat Mass Tran.*, **57** (2013), 582−594. https://doi.org/10.1016/j.ijheatmasstransfer.2012.10.037
8. S. Rashidi, O. Mahian, E. M. Languri, Applications of nanofluids in condensing and evaporating systems, *J. Therm. Anal. Calorim.*, **131** (2018), 2027−2039. https://doi.org/10.1007/s10973-017-6773-7
9. K. Khanafer, K. Vafai, Applications of nanofluids in porous medium, *J. Therm. Anal. Calorim.*, **135** (2019), 1479−1492. https://doi.org/10.1007/s10973-018-7565-4
10. M. A. Nazari, M. H. Ahmadi, M. Sadeghzadeh, M. B. Shafii, M. Goodarzi, A review on application of nanofluid in various types of heat pipes, *J. Cent. South Univ.*, **26** (2019), 1021−1041. https://doi.org/10.1007/s11771-019-4068-9
11. M. U. Sajid, H. M. Ali, Recent advances in application of nanofluids in heat transfer devices: A critical review, *Renew. Sust. Energ. Rev.*, **103** (2019), 556−592. https://doi.org/10.1016/j.rser.2018.12.057
12. A. Wahab, A. Hassan, M. A. Qasim, H. M. Ali, H. Babar, M. U. Sajid, Solar energy systems—Potential of nanofluids, *J. Mol. Liq.*, **289** (2019), 111049. https://doi.org/10.1016/j.molliq.2019.111049
13. D. S. Saidina, M. Z. Abdullah, M. Hussin, Metal oxide nanofluids in electronic cooling: A review, *J. Mater. Sci.-Mater. El.*, **31** (2020), 4381−4398. https://doi.org/10.1007/s10854-020-03020-7
14. J. Li, X. Zhang, B. Xu, M. Yuan, Nanofluid research and applications: A review, *Int. Commun. Heat Mass*, **127** (2021), 105543. https://doi.org/10.1016/j.icheatmasstransfer.2021.105543
15. M. A. Sheremet, Applications of nanofluids, *Nanomaterials (Basel)*, **11** (2021). https://doi.org/10.3390/nano11071716
16. A. Lazarovici, V. Volpert, J. H. Merkin, Steady states, oscillations and heat explosion in a combustion problem with convection, *Eur. J. Mech. B-Fl.*, **24** (2005), 189−203. https://doi.org/10.1016/j.euromechflu.2004.06.007
17. J. H. Merkin, I. Pop, Stagnation point flow past a stretching/shrinking sheet driven by Arrhenius kinetics, *Appl. Math. Comput.*, **337** (2018), 583−590. https://doi.org/10.1016/j.amc.2018.05.024
18. M. M. Rahman, I. Pop, M. Z. Saghir, Steady free convection flow within a titled nanofluid saturated porous cavity in the presence of a sloping magnetic field energized by an exothermic chemical reaction administered by Arrhenius kinetics, *Int. J. Heat Mass Tran.*, **129** (2019), 198−211. https://doi.org/10.1016/j.ijheatmasstransfer.2018.09.105
19. R. H. Muhammad, Analysis of heat transfer in a triangular enclosure filled with a porous medium saturated with magnetized nanofluid charged by an exothermic chemical reaction, *Math. Probl. Eng.*, **2019** (2019), 7451967. https://doi.org/10.1155/2019/7451967

20. M. M. Hasan, M. J. Uddin, R. Nasrin, Exothermic chemical reaction of magneto-convective nanofluid flow in a square cavity, *Int. J. Thermofluids*, **16** (2022), 100236. https://doi.org/10.1016/j.ijft.2022.100236
21. A. Kasaeipoor, B. Ghasemi, S. M. Aminossadati, Convection of Cu-water nanofluid in a vented T-shaped cavity in the presence of magnetic field, *Int. J. Therm. Sci.*, **94** (2015), 50−60. https://doi.org/10.1016/j.ijthermalsci.2015.02.014
22. S. Parvin, A. Akter, Effect of magnetic field on natural convection flow in a prism shaped cavity filled with nanofluid, *Proc. Eng.*, **194** (2017), 421−427. https://doi.org/10.1016/j.proeng.2017.08.166
23. B. P. Geridönmez, H. F. Öztop, Effects of partial magnetic field in a vented square cavity with aiding and opposing of MWCNT—water nanofluid flows, *Eng. Anal. Bound. Elem.*, **133** (2021), 84−94. https://doi.org/10.1016/j.enganabound.2021.08.024
24. A. M. Aly, S. E. Ahmed, Z. Raizah, Impacts of variable magnetic field on a ferrofluid flow inside a cavity including a helix using ISPH method, *Int. J. Numer. Method. H.*, **31** (2021), 2150−2171. https://doi.org/10.1108/HFF-08-2020-0501
25. A. M. Aly, ISPH method for MHD convective flow from grooves inside a nanofluid-filled cavity under the effects of Soret and Dufour numbers, *Physica A*, **546** (2020), 124087. https://doi.org/10.1016/j.physa.2019.124087
26. R. A. Gingold, J. J. Monaghan, Smoothed particle hydrodynamics: theory and application to non-spherical stars, *Mon. Not. R. Astron. Soc.*, **181** (1977), 375−389. https://doi.org/10.1093/mnras/181.3.375
27. L. B. Lucy, A numerical approach to the testing of the fission hypothesis, *The Astron. J.*, **82** (1977), 1013−1024. https://doi.org/10.1086/112164
28. D. Violeau, R. Issa, Numerical modelling of complex turbulent free-surface flows with the SPH method: an overview, *Int. J. Numer. Method. Fl.*, **53** (2007), 277−304. https://doi.org/10.1002/fld.1292
29. H. F. Qiang, C. Shi, F. Z. Chen, Y. W. Han, Simulation of two-dimensional droplet collisions based on SPH method of multi-phase flows with large density differences, *Acta Phys. Sin.*, **62** (2013), 214701. https://doi.org/10.7498/aps.62.214701
30. A. M. Aly, A. J. Chamkha, S. W. Lee, A. F. Al-Mudhaf, On mixed convection in an inclined lid-driven cavity with sinusoidal heated walls using the ISPH method, *Comput. Therm. Sci. Int. J.*, **8** (2016), 337−354. https://doi.org/10.1615/ComputThermalScien.2016016527
31. F. Garoosi, A. Shakibaeinia, An improved high-order ISPH method for simulation of free-surface flows and convection heat transfer, *Powder Technol.*, **376** (2020), 668−696. https://doi.org/10.1016/j.powtec.2020.08.074
32. Y. Shimizu, H. Gotoh, A. Khayyer, K. Kita, Fundamental investigation on the applicability of higher-order consistent ISPH method, *Int. J. Offshore Polar Eng.*, 2022. https://doi.org/10.17736/ijope.2022.jc868
33. N. H. Saeid, Natural convection in a square cavity with discrete heating at the bottom with different fin shapes, *Heat Transfer Eng.*, **39** (2018), 154−161. https://doi.org/10.1080/01457632.2017.1288053
34. A. M. Aly, S. El-Sapa, Effects of Soret and Dufour numbers on MHD thermosolutal convection of a nanofluid in a finned cavity including rotating circular cylinder and cross shapes, *Int. Commun. Heat Mass*, **130** (2022), 105819. https://doi.org/10.1016/j.icheatmasstransfer.2021.105819
35. L. El Moutaouakil, M. Boukendil, Z. Zrikem, A. Abdelbaki, Natural convection and surface radiation heat transfer in a cavity with vertically oriented fins, *Mater. Today Proc.*, **27** (2020), 3051−3057. https://doi.org/10.1016/j.matpr.2020.03.526

36. M. M. Tafarroj, O. Mahian, A. Kasaeian, K. Sakamatapan, A. S. Dalkilic, S, Wongwises, Artificial neural network modeling of nanofluid flow in a microchannel heat sink using experimental data, *Int. Commun. Heat Mass*, **86** (2017), 25−31. https://doi.org/10.1016/j.icheatmasstransfer.2017.05.020
37. H. M. Elshehabey, A. M. Aly, S. W. Lee, A. B. Çolak, Integrating artificial intelligence with numerical simulations of Cattaneo-Christov heat flux on thermosolutal convection of nano-enhanced phase change materials in Bézier-annulus, *J. Energy Storage*, **82** (2024), 110496. https://doi.org/10.1016/j.est.2024.110496
38. A. M. Aly, S. W. Lee, N. N. Ho, Z. Raizah, Thermosolutal convection of NEPCM inside a curved rectangular annulus: Hybrid ISPH method and machine learning, *Comput. Part. Mech.*, **11** (2024), 2655–2675. https://doi.org/10.1007/s40571-024-00744-9
39. I. E. Lagaris, A. Likas, D. I. Fotiadis, Artificial neural networks for solving ordinary and partial differential equations, *IEEE T. Neural Networ.*, **9** (1998), 987−1000. https://doi.org/10.1109/72.712178
40. G. Diaz, M. Sen, K. T. Yang, R. L. McClain, Simulation of heat exchanger performance by artificial neural networks, *HVAC&R Res.*, **5** (1999), 195−208. https://doi.org/10.1080/10789669.1999.10391233
41. Y. Varol, E. Avci, A. Koca, H. F. Oztop, Prediction of flow fields and temperature distributions due to natural convection in a triangular enclosure using Adaptive-Network-Based Fuzzy Inference System (ANFIS) and Artificial Neural Network (ANN), *Int. Commun. Heat Mass*, **34** (2007), 887−896. https://doi.org/10.1016/j.icheatmasstransfer.2007.03.004
42. S. Motahar, A neural network approach to estimate non-Newtonian behavior of nanofluid phase change material containing mesoporous silica particles, *Int. J. Eng.*, **34** (2021), 1974−1981. https://doi.org/10.5829/ije.2021.34.08b.18
43. W. Alhejaili, S. W. Lee, C. Q. Hat, A. M. Aly, Heat and mass transport of nano-encapsulated phase change materials in a complex cavity: An artificial neural network coupled with incompressible smoothed particle hydrodynamics simulations, *AIMS Math.*, **9** (2024), 5609−5632. https://doi.org/10.3934/math.2024271
44. H. M. Elshehabey, A. B. Çolak, A. Aly, Adjoined ISPH method and artificial intelligence for thermal radiation on double diffusion inside a porous L-shaped cavity with fins, *Int. J. Numer. Method. H.*, **34** (2024), 1832−1857. https://doi.org/10.1108/HFF-11-2023-0677
45. S. I. Abdelsalam, N. Alsedais, A. M. Aly, Revolutionizing bioconvection: Artificial intelligence-powered nano-encapsulation with oxytactic microorganisms, *Eng. Appl. Artif. Intel.*, **137** (2024), 109128. https://doi.org/10.1016/j.engappai.2024.109128
46. M. T. Nguyen, A. M. Aly, S. W. Lee, Effect of a wavy interface on the natural convection of a nanofluid in a cavity with a partially layered porous medium using the ISPH method, *Numer. Heat Tr. A-Appl.*, **72** (2017), 68−88. https://doi.org/10.1080/10407782.2017.1353385
47. M. T. Nguyen, A. M. Aly, S. W. Lee, ISPH modeling of natural convection heat transfer with an analytical kernel renormalization factor, *Meccanica*, **53** (2018), 2299−2318. https://doi.org/10.1007/s11012-018-0825-3
48. A. M. Aly, E. M. Mohamed, N. Alsedais, The magnetic field on a nanofluid flow within a finned cavity containing solid particles, *Case Stud. Therm. Eng.*, **25** (2021), 100945. https://doi.org/10.1016/j.csite.2021.100945
49. G. R. Kefayati, FDLBM simulation of mixed convection in a lid-driven cavity filled with non-Newtonian nanofluid in the presence of magnetic field, *Int. J. Therm. Sci.*, **95** (2015), 29−46. https://doi.org/10.1016/j.ijthermalsci.2015.03.018

50. Y. Xuan, W. Roetzel, Conceptions for heat transfer correlation of nanofluids, *Int. J. Heat Mass Tran.*, **43** (2000), 3701−3707. https://doi.org/10.1016/S0017-9310(99)00369-5
51. T. Mahapatra, B. C. Saha, D. Pal, Magnetohydrodynamic double-diffusive natural convection for nanofluid within a trapezoidal enclosure, *Comput. Appl. Math.*, **37** (2018), 6132−6151. https://doi.org/10.1007/s40314-018-0676-5
52. T. M. Nguyen, A. M. Aly, S. W. Lee, ISPH modeling of natural convection heat transfer with an analytical kernel renormalization factor, *Meccanica*, **53** (2018), 2299–2318. https://doi.org/10.1007/s11012-018-0825-3
53. T. M. Nguyen, A. M. Aly, S. W. Lee, Improved wall boundary conditions in the incompressible smoothed particle hydrodynamics method, *Int. J. Numer. Method. H. F. F.*, **28** (2018), 704−725. https://doi.org/10.1108/HFF-02-2017-0056
54. A. M. Aly, Z. A. S. Raizah, Mixed convection in an inclined nanofluid filled-cavity saturated with a partially layered porous medium, *J. Therm. Sci. Eng. Appl.*, **11** (2019), 041002−041011. https://doi.org/10.1115/1.4042352
55. S. J. Lind, R. Xu, P. K. Stansby, B. D. Rogers, Incompressible smoothed particle hydrodynamics for free-surface flows: A generalised diffusion-based algorithm for stability and validations for impulsive flows and propagating waves, *J. Comput. Phys.*, **231** (2012), 1499−1523. https://doi.org/10.1016/j.jcp.2011.10.027
56. A. Skillen, S. Lind, P. K. Stansby, B. D. Rogers, Incompressible smoothed particle hydrodynamics (SPH) with reduced temporal noise and generalised Fickian smoothing applied to body-water slam and efficient wave-body interaction, *Comput. Method. Appl. M.*, **265** (2013), 163−173. https://doi.org/10.1016/j.cma.2013.05.017
57. M. T. Nguyen, A. M. Aly, S. W. Lee, Natural convection in a non-Darcy porous cavity filled with Cu-water nanofluid using the characteristic-based split procedure in finite-element method, *Numer. Heat Tr. A-Appl.*, **67** (2015), 224−247. https://doi.org/10.1080/10407782.2014.923225
58. G. V. Davis, Natural convection of air in a square cavity: A bench mark numerical solution, *Int. J. Numer. Meth. Fl.*, **3** (1983), 249−264. https://doi.org/10.1002/fld.1650030305
59. A. B. Çolak, A new study on the prediction of the effects of road gradient and coolant flow on electric vehicle battery power electronics components using machine learning approach, *J. Energy Storage*, **70** (2023), 108101. https://doi.org/10.1016/j.est.2023.108101
60. A. B. Çolak, O. Yıldız, M. Bayrak, B. S. Tezekici, Experimental study for predicting the specific heat of water based Cu-Al_2O_3 hybrid nanofluid using artificial neural network and proposing new correlation, *Int. J. Energ. Res.*, **44** (2020), 7198−7215. https://doi.org/10.1002/er.5417

AIMS Press